Nonlinear Processes in Geophysics, 12, 603–623, 2005
SRef-ID: 1607-7946/npg/2005-12-603
European Geosciences Union

Nonlinear Processes in Geophysics

A simplified model of the Martian atmosphere – Part 1: a diagnostic analysis

S. G. Whitehouse[1], **S. R. Lewis**[2], **I. M. Moroz**[1], **and P. L. Read**[2]

[1]Mathematical Institute, University of Oxford, UK
[2]Atmospheric, Oceanic & Planetary Physics, Clarendon Laboratory, University of Oxford, UK

Received: 9 December 2004 – Revised: 22 March 2005 – Accepted: 11 April 2005 – Published: 17 June 2005

Abstract. In this paper we derive a reduced-order approximation to the vertical and horizontal structure of a simplified model of the baroclinically unstable Martian atmosphere. The original model uses the full hydrostatic primitive equations on a sphere, but has only highly simplified schemes to represent the detailed physics of the Martian atmosphere, e.g. forcing towards a plausible zonal mean temperature state using Newtonian cooling. Three different norms are used to monitor energy conversion processes in the model and are then compared. When four vertical modes (the barotropic and first three baroclinic modes) are retained in the reduced-order approximation, the correlation norm captures approximately 90% of the variance, while the kinetic energy and total energy norms capture approximately 83% and 78% of the kinetic and total energy respectively. We show that the leading order Proper Orthogonal Decomposition (POD) modes represent the dominant travelling waves in the baroclinically-unstable, winter hemisphere. In part 2 of our study we will develop a hierarchy of truncated POD-Galerkin expansions of the model equations using up to four vertical modes.

1 Introduction

Mars is one of the terrestrial planets, having a relatively thin atmosphere in terms of physical depth, composed primarily of carbon dioxide with small amounts of other gases, and covering a solid surface. The inclination of the Martian polar axis to the ecliptic plane (25.2° compared to 23.9° for Earth) implies that Mars has seasons like the Earth. Both are rapidly rotating planets, rotating at about the same speed (the Martian day is 24 h 39.4 m), so that Coriolis forces will have similar magnitudes. Much of the water on Mars is believed to be in the permafrost beneath the surface, leading to low observed atmospheric concentrations. There is insufficient water vapour to permit large amounts of latent heat release in convective clouds, but absorption of short wave radiation by suspended dust in the lower and middle atmosphere can produce significant local heating rates (Gierasch and Goody, 1972; Pollack et al., 1979). This results in a fundamental difference between the two planetary circulations with the Martian circulation driven primarily by the heating of the surface and dust suspended in the atmosphere.

Spacecraft observations, notably those made by the Viking Landers, have provided evidence for the existence of transient baroclinic eddies in the atmosphere of Mars. Such waves have been thought to exist since the work of Hess (1950), and their occurrence was confirmed by the work of Barnes (1980, 1981), who showed that the oscillations were often regular and repeatable, and that, by assuming the waves were geostrophic and sinusoidal, typically flows were dominated by wavenumbers 3 and 4 with phase speeds between 15–16 ms^{-1}. Barnes et al. (1993) studied the baroclinic wave activity using the NASA Ames Mars model and found that zonal wavenumbers 1–4 with periods 2–10 days existed, and that such oscillations were regular in time. Collins et al. (1996) found evidence for dominant baroclinic modes at wavenumbers 1 and 2 in the Oxford Mars General Circulation Model (MGCM), with similar periods to waves detected in the Viking Lander surface pressure data. More recently Banfield et al. (2004) have shown the presence of strong wavenumber 1, and to a lesser extent 2 and 3, travelling waves in thermal remote sensing observations from the Mars Global Surveyor spacecraft.

The autumn, winter and spring circulation of the Martian atmosphere is dominated by these heat transporting baroclinic transients; during the summer only small fluctuations of pressure, other than internal tides, occur and no travelling waves are typically observed in either hemisphere.

Flows observed in the Earth's atmosphere and in laboratory models of hydrodynamical systems often provide evidence of behaving as if they have a relatively small number of degrees of freedom. Selten (1993) introduced a two-level quasi-geostrophic hemi-spherical model of the Earth's atmosphere, formulated in spherical harmonics with vertical

Correspondence to: I. M. Moroz
(moroz@maths.ox.ac.uk)

Empirical Orthogonal Functions (EOFs) to describe the evolution of the circulation. The EOFs were calculated using either a kinetic energy (KE) or a total energy (TE) norm, and evolution equations for their amplitudes were derived by the Galerkin projection of the model equations onto the EOF basis. He found that the global structure of the system could only be described in a truncated TE model since the KE model failed to simulate adequately the energy conversion processes which are fundamental to baroclinic flows.

In a similar study of simplified Earth-like circulations, Selten (1995) used a T21 spectral barotropic model and showed that it could be accurately modelled by using just 20 EOFs, which were computed in spectral space, while Selten (1997) concluded that an EOF basis is more efficient at describing large-scale atmospheric dynamics compared to spherical harmonics. However this was not the case for the baroclinic model.

The main objective of this paper is to seek a low-dimensional description of a baroclinically unstable atmosphere, under conditions appropriate to Mars, by deriving a reduced-order approximation of the vertical and horizontal structure of the system, retaining only the dominant baroclinic and barotropic modes. Then (in Part II of our study) we shall combine this with a POD-Galerkin expansion of the model equations. The POD or Proper Orthogonal Decomposition method is a procedure for calculating the eigenvectors (called the POD modes) of the time-averaged autocorrelation function of a given time series $\mathbf{v}(\mathbf{x}, t)$ (Lumley, 1967, 1981). The resulting eigenvectors are optimal, in the sense of energy capture. The corresponding eigenvalues are measures of the variance contained in each mode and describe the relative energy content of each POD mode.

The vertical modes will be obtained, in Sect. 3, via the solution of a variational problem for data from a numerical model and corresponding to a wave number 3 observed during winter in the Martian southern hemisphere (SH).

Reducing the system to its essential degrees of freedom may provide useful insight into the underlying physical processes which occur in the original model, revealing the dominant interactions between the various modes and their contributions to atmospheric variability on various timescales. Dynamical systems methods will then be employed to analyse the resulting bifurcations.

2 The SGCM

The numerical model in question is that of Collins and James (1995) and is known hereafter as the Simple General Circulation Model (SGCM). The SGCM is an idealised model in which the adiabatic, hydrostatic primitive equations of meteorology, as described by Hoskins and Simmons (1975), are solved in spherical coordinates using a spectral representation in the horizontal and finite-difference σ-coordinates in the vertical, (where $\sigma = p(\theta, \phi, z, t)/p_*(\theta, \phi, t)$, p=pressure, p_*=surface pressure, θ is latitude, ϕ longitude, z height and t time) with simplified physical parameterisations of heating and friction. The spectral primitive equation model employs a triangular truncation at total horizontal wavenumber 21 (denoted T21) and has 10 equally spaced σ levels in the vertical over a pressure range of 0 to 610 Pa. Surface drag is represented by Rayleigh friction in the lowest layer with a time-scale of 3 days (denoted τ_D). Heating is modelled as Newtonian relaxation toward a zonally symmetric equilibrium temperature distribution with a time-scale of 2 days (representing a typical radiative relaxation timescale on Mars and denoted τ_E). For simplicity topography was excluded in the model in order that the baroclinic waves could be isolated and would not suffer from orographic modulation (although this is likely to be important for the real waves on Mars).

2.1 Selecting the governing equations

In selecting the set of governing equations to form the basis of the POD-Galerkin reduced models which best suits our requirements, we want the equations to describe the flow, but not be excessively computationally intensive. If the original primitive equations are used as the governing equations, then the computations become too large for simple algorithms, and the retrieval of the eigenvalues and eigenvectors of the autocorrelation matrix (in order to compute the POD modes) could only be achieved by using sophisticated and expensive algorithms such as the Iterative Lanzcos Algorithm (ILA). Buizza and Palmer (1995) remark that the ILA is intended to compute a few of the eigenvalues and corresponding eigenvectors of a large symmetric matrix and is applied to large, sparse, symmetric eigenvalue-problems. Although the highly truncated system which we investigate satisfies this criterion, the adjoint operator must also be coded, itself a formidable task. An alternative and simpler approach involves the formulation of the quasi-geostrophic (QG) equations on a sphere.

2.2 Martian atmospheric behaviour and QG theory

Mars is a rapidly rotating planet, with maximum wind speeds reaching $O(100)\ \mathrm{ms}^{-1}$ at a height of 30–50 km above the surface. This suggests that the Rossby number, $Ro = U/fL$, is much less than unity for large scales $>$ 1000 km. This is important since it suggests the QG approximation holds for atmospheric motions with frequencies $<\Omega$, the angular frequency of the planet (Andrews et al., 1987). The equations used will retain the full Coriolis parameter, $f = 2\Omega \sin\theta$, where Ω is the angular speed of the rotating planet and θ is the latitude. By including f we consider large-scale, essentially geostrophic motions on a sphere.

If L is the horizontal scale and a the planetary radius, the restriction to small L/a permits the QG equations on a sphere to be used as the governing set of equations for our investigations.

3 The vertical structures

In this section we discuss how to derive a set of normal modes to model the vertical structure using data generated from the numerical model. If a poor vertical scheme is used then important information concerning physical processes and energy exchanges may not be captured in the POD-Galerkin model.

The separable solution approach was used by Flierl (1978) in an oceanographic context. He showed that linear eigenmodes in a system with horizontal boundaries are integrated functions of N^2 (the Brunt-Vaïsälä frequency see below). In a system with homogeneous boundary conditions, a simple Sturm-Liouville problem has to be solved in order to obtain the normal modes. In practice it is found that the barotropic and the first few baroclinic modes are the most significant (and consistent with the two modes generally represented by well-calibrated two-layer or two-level quasi-geostrophic models).

3.1 The QG vertical structure equation

The adiabatic, frictionless Quasi-Geostrophic Potential Vorticity (QGPV) equation in isobaric coordinates takes the form

$$\frac{D_g q}{Dt} = \left(\frac{\partial}{\partial t}+\mathbf{V}_g \cdot \nabla_h\right)\left(\frac{1}{f_0}\nabla_h^2\Phi+f_0\frac{\partial}{\partial p}\left(\frac{1}{S}\frac{\partial\Phi}{\partial p}\right)+f\right) = 0, \quad (1)$$

where $D_g/Dt=\partial/\partial t+\mathbf{V}_g \cdot \nabla_h$ is the derivative following the geostrophic flow and q is the QGPV defined by

$$q = \left(\frac{1}{f_0}\nabla_h^2\Phi + f_0\frac{\partial}{\partial p}\left(\frac{1}{S}\frac{\partial\Phi}{\partial p}\right)+f\right). \quad (2)$$

The horizontal Laplacian is defined as

$$\nabla_h^2 = \frac{1}{a^2}\left(\frac{\partial^2}{\partial\theta^2}+\frac{1}{\cos^2\theta}\frac{\partial^2}{\partial\phi^2}\right), \quad (3)$$

longitude. The geostrophic component of velocity is $\mathbf{V}_g=(\mathbf{k}\wedge\nabla_h\Phi)/f$ where $\mathbf{k}$ is the unit vector in the vertical direction, $\Phi(\theta,\phi,p,t)$ is the isobaric distribution of the geopotential and p is pressure. The geostrophic vorticity term is $\xi_g=\nabla_h^2(\Phi/f_0)$, where f_0 is a synoptic scale of motion for the Coriolis parameter. Finally, the stratification profile is $S=N^2/(g^2\rho^2)$, where g is the acceleration due to gravity, ρ is density and

$$N^2 = -\frac{g^2\rho}{\theta_0}\left(\frac{\partial\theta_0}{\partial p}\right) = -\frac{g^2 P}{RT\theta_0}\left(\frac{\partial\theta_0}{\partial p}\right), \quad (4)$$

is the Brunt-Vaïsälä frequency in isobaric coordinates, where θ_0 is the potential temperature surface from equilibrium; T is temperature and R is the gas constant for dry air.

Writing Φ in separable form as $\Phi=\sum_i \widetilde{\Phi}_i(\theta,\phi,t)H_i(p)$ and substituting into Eq. (1), we find that the vertical structure equation to be solved is

$$f_0{}^2\frac{d}{dp}\left(\frac{1}{S}\frac{dH_i}{dp}\right)+\lambda_i H_i = 0, \quad (5)$$

with homogeneous boundary conditions

$$\frac{dH_1}{dp}|_{p_1} = \frac{dH_1}{dp}|_{p_n} = 0, \quad (6)$$

where the λ_is in Eq. (5) form a discrete countable set of eigenvalues, S is the stratification profile and p_1, p_n are pressures at the upper and lower boundaries respectively. The H_is form a complete orthogonal set and can be orthonormalised by setting

$$\frac{1}{P}\int_{p_1}^{p_n} H_i(p)H_j(p)dp = \delta_{ij}, \quad (7)$$

where P is the pressure difference between the two boundaries.

3.2 The Froude number

The Rossby radius of deformation (R_d) is the characteristic length scale of disturbances in the mid-latitudes (e.g. James, 1994) and can be interpreted as the horizontal length scale over which the geopotential height field adjusts whilst approaching geostrophic equilibrium. In the derivation of Eq. (5), $R_{d_i}=1/\sqrt{\lambda_i}$ is the relevant Rossby Radius of deformation for each mode. If the Froude number is defined as $F=\frac{a^2}{R_d^2}$, Eq. (5) therefore provides a spectrum of Froude numbers $\{F_i\}$, where each Froude number F_i corresponds to a different vertical scaling. Therefore, $a^2\lambda_0$ represents the Froude number of the barotropic mode, $a^2\lambda_1$ the Froude number of the first baroclinic mode, and so on. The global Froude number for the SGCM is taken to be $F=a^2\lambda_1$ since the vertical length scale of the first baroclinic mode is the depth of the planetary model. Hence S_i will be replaced by S, with the understanding that $i=1$.

3.3 Definitions of energy

To derive vertical normal modes which are solutions to the linearised vorticity equation we assume a separable form for the streamfunction:

$$\psi(\theta,\phi,p,t) = \sum_{l=0}^{\infty}\widetilde{\psi}_l(\theta,\phi,t)H_l(p), \quad (8)$$

so that the total KE of the system on a sphere of radius a becomes:

$$KE = \frac{1}{2}\int_0^{\pi}\int_0^{2\pi}\int_{p_1}^{p_n}(\nabla_h\psi\cdot\nabla_h\psi)\,a^2\sin\theta dp d\phi d\theta = \frac{1}{2}\int_0^{\pi}\int_0^{2\pi}\sum_{l=0}^{\infty}\left|\nabla_h(\widetilde{\psi}_l)\right|^2 a^2\sin\theta d\phi d\theta, \quad (9)$$

where $\int_{p_1}^{p_n}H_l H_m dp=\delta_{lm}$ is assumed and p_1, p_n are the pressures at the upper and lower boundaries respectively.

Taking $H_0(p)$ to be the barotropic mode and $H_k(p)$ to be the k-th baroclinic mode (for $k\neq 0$), following Selten (1993),

the contribution to the available potential energy (APE) from the k-th baroclinic mode is:

$$\begin{aligned} &APE_k \\ &= \int_0^{\pi}\int_0^{2\pi}\int_{p_1}^{p_n}\left(\frac{{f_0}^2}{S}\left(\frac{dH_k}{dp}\right)^2\right)_k \widetilde{\psi}_k^2 a^2 \sin\theta dp d\phi d\theta \\ &= \int_0^{\pi}\int_0^{2\pi}\left(\frac{{f_0}^2}{S}\left(\frac{dH_k}{dp}\right)\right)_k \frac{dH_k}{dp}]_{p_1}^{p_n}\widetilde{\psi}_k^2 a^2 \sin\theta d\phi d\theta \\ &- \int_0^{\pi}\int_0^{2\pi}\int_{p_1}^{p_n}\frac{d}{dp}\left(\frac{{f_0}^2}{S}\left(\frac{dH_k}{dp}\right)\right)_k H_k\widetilde{\psi}_k^2 a^2 \sin\theta dp d\phi d\theta. \end{aligned} \tag{10}$$

Assuming that $\frac{dH_k}{dp}|_{p_1}=\frac{dH_k}{dp}|_{p_n}=0$, we obtain:

$$APE_k = \int_0^{\pi}\int_0^{2\pi}\int_{p_1}^{p_n}\lambda_k\left(H_k\widetilde{\psi}_k\right)^2 a^2 \sin\theta dp d\phi d\theta, \tag{11}$$

where the subscript k refers to the k-th mode.

3.4 The vertical modes

We begin by showing that Eq. (5) can be derived from a variational principle in which we minimise APE in the vertical direction. If we assume that $\Phi=\widetilde{\Phi}(\theta,\phi,t)H(p)$, then the APE integrand is proportional to $\frac{{f_0}^2}{S}(\frac{dH}{dp})^2$, as above. The variational problem becomes that of seeking stationary solutions to the APE functional:

$$I[H] = \int_{p_1}^{p_n}\frac{{f_0}^2}{S}\left(\frac{dH}{dp}\right)^2 dp, \tag{12}$$

subject to the constraint:

$$J[H] = \int_{p_1}^{p_n} H^2 dp = 1, \tag{13}$$

together with Eq. (6). The original SGCM has an artificial "sponge" level at the upper boundary (in order to reduce the problems of spurious energy reflection) and so the vertical modes satisfying these constraints are perfectly consistent.

Using standard Calculus of Variations, the Euler-Lagrange equation becomes:

$$f_0^2\frac{d}{dp}\left(\frac{1}{S}\frac{dH}{dp}\right) = -\gamma H, \tag{14}$$

where γ is the Lagrange multiplier to be determined (c.f. Eq. (5) if we identify γ with λ) or

$$\mathcal{L}H = \lambda H, \tag{15}$$

where $\mathcal{L}=-\frac{d}{dp}\left[\frac{f_0^2}{S(p)}\frac{d}{dp}\right]$. Since f_0 is independent of p we have an eigenvalue problem, where H is the eigenfunction corresponding to the eigenvalue λ.

Defining $F=\frac{f_0^2}{S}(\frac{dH}{dp})^2$ and $E=\frac{\partial^2 F}{\partial H'^2}-\lambda\frac{\partial^2 H^2}{\partial H'^2}$, where $H'=\frac{dH}{dp}$, then $E=\frac{2f^2}{S}>0$ implies that $I[H]$ has a minimum within the range of integration.

This is mathematically significant since, if total energy (TE) in the system is invariant, then minimising APE maximises KE. The first eigenmode which is derived from Eq. (15) is the barotropic mode which, by definition, contains no APE but instead captures almost all of the KE of the system. The remaining modes will then tend to contribute progressively less to the total KE of the system.

From Sturm-Liouville theory (for example see Mikhlin, 1964), since $\frac{{f_0}^2}{S}\geq 0$ and $\int_{p_1}^{p_n}(\frac{{f_0}^2}{S})^{-1}dp$ is bounded, we have

$$|H|_e^2 = \int_{p_1}^{p_n}\frac{f_0^2}{S}\left(\frac{dH}{dp}\right)^2 dp = \lambda_n, \tag{16}$$

where $|H|_e$ is the energy norm of function H. This is identical to the vertical component of the APE norm used in Eq. (10), where

$$\begin{aligned}[H_n, H_m]_e &= \int_{p_1}^{p_n}\frac{f_0^2}{S}\left(\frac{dH_n}{dp}\right)\left(\frac{dH_m}{dp}\right)dp \\ &= \lambda_n\delta_{nm}, \end{aligned} \tag{17}$$

shows the orthogonality of H_n with respect to the energy norm. The set $\{H_n(p)\}_{n=1}^{\infty}$ is complete both in terms of energy and in the sense of convergence in the mean.

Multiplying both sides of Eq. (14) by H and integrating by parts we obtain

$$\lambda = \int_{p_1}^{p_n}\frac{{f_0}^2}{S}\left(\frac{dH}{dp}\right)^2 dp \Big/ \int_{p_1}^{p_n} H^2 dp, \tag{18}$$

where we have used Eq. (6). Therefore all non-zero λ's are positive. We note that $\lambda=0$ is satisfied if $H=1$ and corresponds to the purely barotropic mode.

We remark here that, since we are solving an atmospheric problem, the upper boundary condition should be made more realistic. Indeed, Lindzen et al. (1968) showed that bounded atmospheric models could produce spurious free oscillations and concluded that bounded atmospheres do not properly respond to oscillations which propagate vertically. However, for the purpose of this present study, the vertical structure equation is solved with homogeneous boundary conditions.

4 The SGCM data

The SGCM with its simplified parameterisations of heating and friction and the absence of topography has been used to examine a baroclinic wave number 3 flow during a continual seasonal numerical simulation of the southern hemisphere Martian winter (Collins and James, 1995).

4.1 The decomposition

By assuming a decomposition of the streamfunction ψ to be possible in separable form, the amplitude distribution $\widetilde{\psi}_m(\theta,\phi)$ of baroclinic mode m can be calculated for each

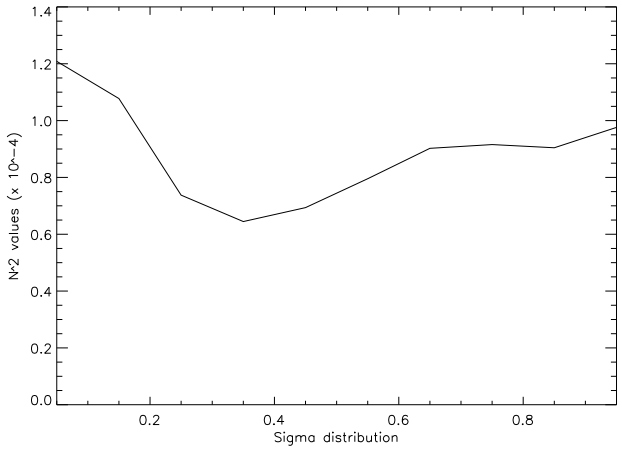

Fig. 1. The buoyancy frequency profile, N^2, at 52.6° S in the SGCM.

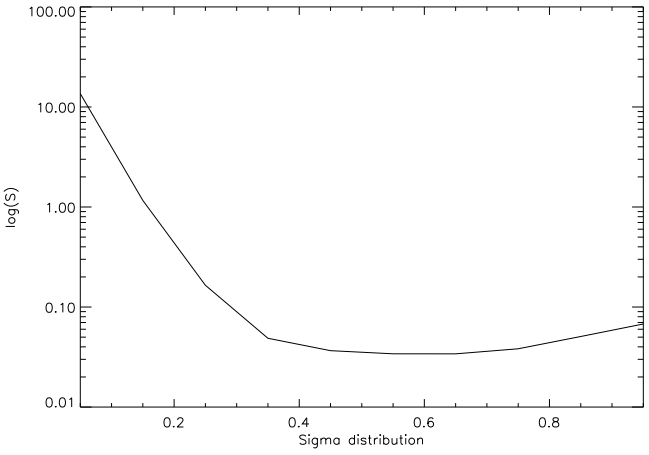

Fig. 2. The stratification parameter, S, at 52.6° S.

profile, as a function of θ, ϕ or profile location. If ψ_j is the streamfunction for level j, then

$$\psi_j = \sum_{m=1}^{N} \widetilde{\psi}_m \mathbf{H}_m(\sigma_j), \tag{19}$$

where $\mathbf{H}_i(\sigma_j)$ is the i-th vertical mode in layer σ_j. The spectral primitive equation model has 10 equally spaced σ levels, where $\sigma = p/p_s$, where p_s is the surface pressure, as defined earlier. It is therefore convenient to calculate the normal modes on these surfaces; σ_j refers to the jth level (see Table 1). N is the number of vertical levels (and hence the total number of normal modes).

The orthonormality condition of $\mathbf{H}_i$ becomes

$$\frac{1}{P} \sum_{j=1}^{N} \delta\sigma_j \mathbf{H}_i(\sigma_j) \mathbf{H}_k(\sigma_j) = \delta_{ik}, \tag{20}$$

where $P = \sum_{i=1}^{N} \sigma_i$. Since the difference in σ between two consecutive sigma surfaces is fixed (see Table 1), $\delta\sigma_j$ is constant, so that

$$\mathbf{H}_k \mathbf{H}_k^T = N\mathbf{I}, \tag{21}$$

where $\mathbf{I}$ is the identity matrix. Thus

$$\widetilde{\psi}_m = \frac{1}{N} \sum_{j=1}^{N} < \mathbf{H}_m(\sigma_j), \psi_j > . \tag{22}$$

We are thus able to calculate the KE and APE in each of the modes.

The N^2 profile at latitude 52.61° S is shown in Fig. 1, while the corresponding stratification parameter profile is shown in Fig. 2. Because the streamfunction has a dominant steady wave 3 in the southern hemisphere latitude band 40° S–60° S (see Figs. 3 and 4), the stratification was averaged over this interval, because of the significant atmospheric activity there. The normal modes were optimised over this chosen band.

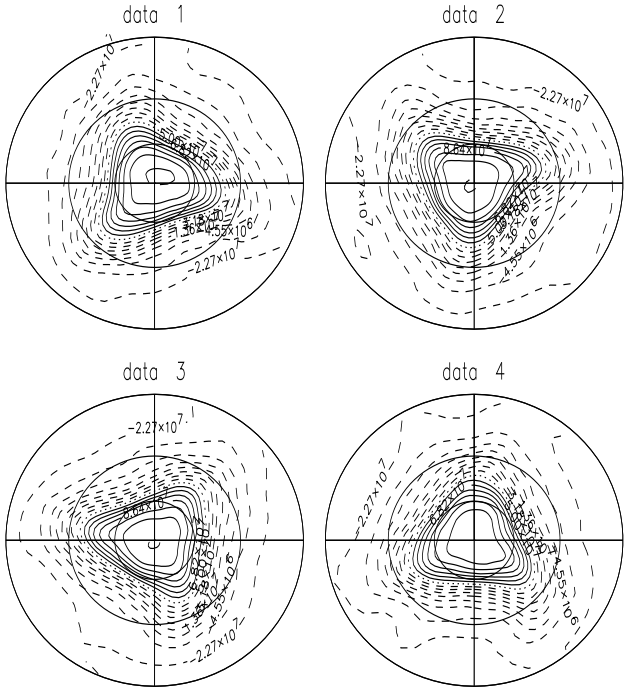

Fig. 3. Southern hemisphere stereographic projection maps of the SGCM modelled streamfunction data during the southern winter solstice (L_S=90°). The steady wave 3 streamfunction is shown at the first 4 days on σ=0.45.

4.2 Eigenvalues and eigenmodes

Figure 4 shows the decomposition of the SGCM streamfunction into its purely barotropic and nine baroclinic components. Shown in Fig. 4a are the barotropic and first three baroclinic components during the first day. The barotropic component can be viewed as an equal-weighted averaged flow over the vertical levels, which reveals a steady wave flow between 40° S–60° S. The first and second baroclinic components contain modulated wave three profiles in the

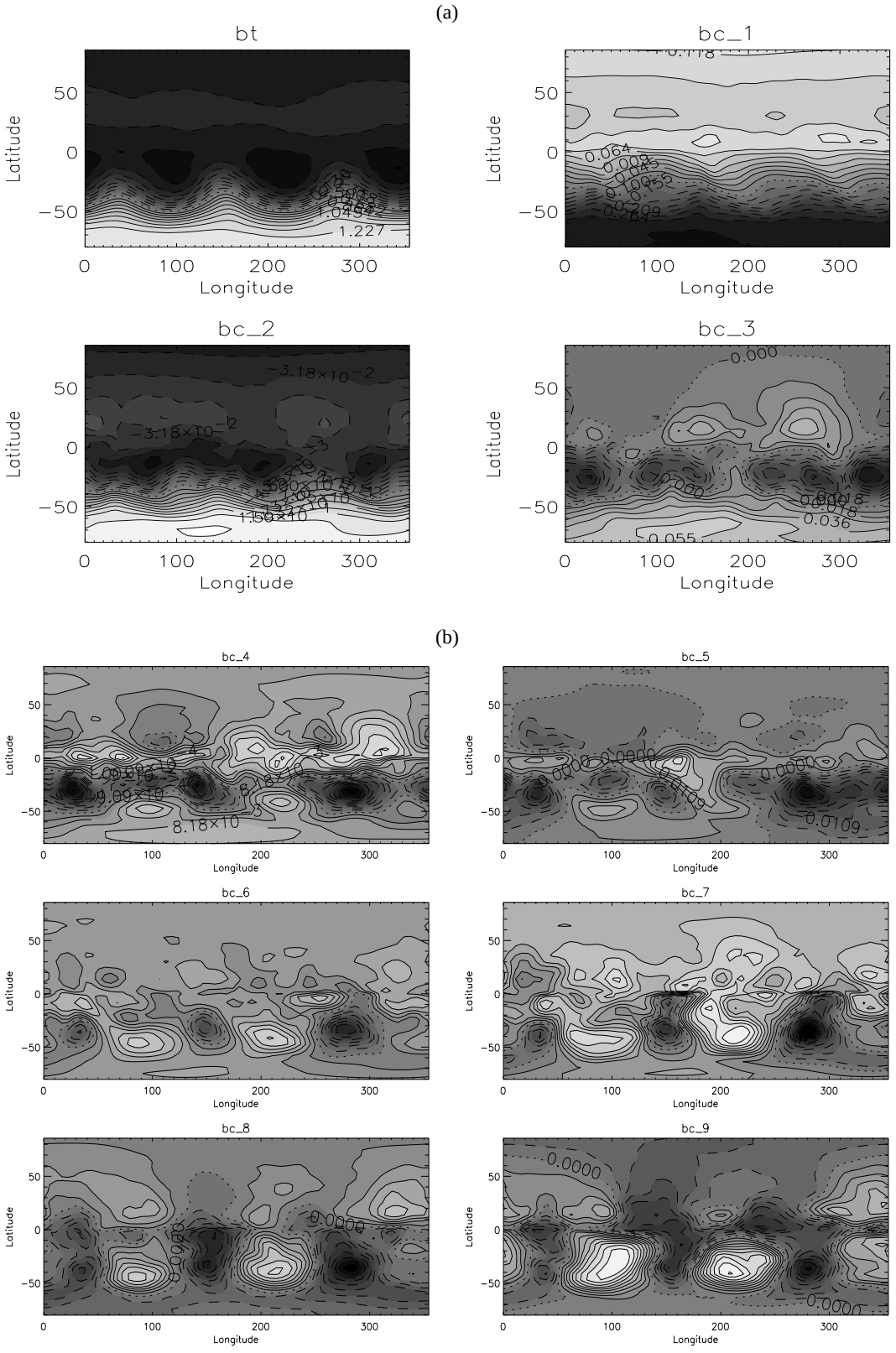

Fig. 4. Decomposition of the SGCM streamfunction data into its purely barotropic and nine baroclinic components. The figure illustrates the instantaneous fields of **(a)** the purely barotropic and first three baroclinic components and **(b)** baroclinic components 4 to 9.

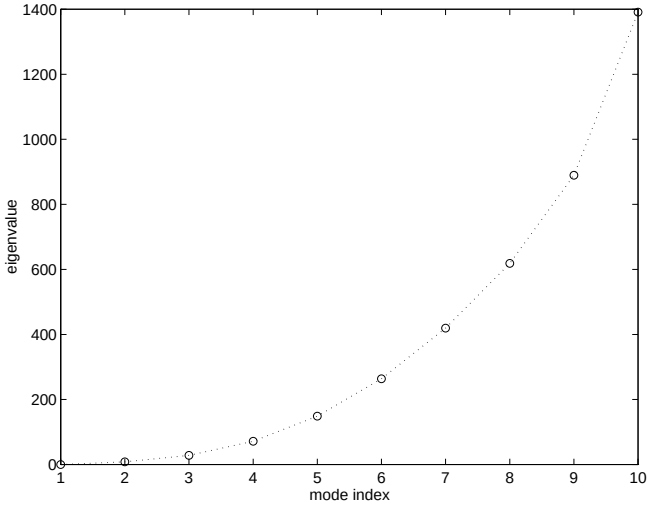

Fig. 5. Froude numbers calculated from the vertical structure equation for the stability profile shown in Fig. 1.

SH, whereas the third component possesses a baroclinic wavenumber 3 structure, centred at a latitude of 30° S and surrounded by a more complicated flow. Figure 4b shows the instantaneous baroclinic components 4 to 9. Baroclinic modes 4 to 7 contain wavenumber 3 structures, centred at a latitude of 50° S, while baroclinic modes 8 and 9 have wavenumber 2 structures at a latitude of 45° S.

The eigenvalues λ_k, computed from Eq. (5), can be expressed as an increasing sequence (see Table 1) or shown graphically (see Fig. 5).

Figure 6 shows the corresponding eigenmodes, identified as the purely barotropic mode (corresponding to λ_0=0) and the nine baroclinic modes (b)–(j). Table 1 also gives the values of the Rossby radius of deformation for each eigenmode and the corresponding values of Froude number. For any $k>0$, $\mathbf{H}_k$ has one more zero in the interval (σ_1, σ_{10}) than does $\mathbf{H}_{k-1}$.

The purely barotropic mode takes the value unity at all vertical levels, while the first two baroclinic modes have a dominant baroclinic structure near the top of the model. The vertical structures become progressively more complicated for the higher order modes, particularly near the ground level.

4.3 Energy distributions

Figure 7 shows the relative contributions to KE, APE and TE from each of the 10 eigenmodes. The purely barotropic eigenmode represents 89% of the total KE, whereas the first and second baroclinic eigenmodes supplement KE by just 6.1% and 2.5%, respectively. The remaining modes contribute progressively less to the total KE except for baroclinic modes 8 and 9 which contain 0.19% and 0.20% of KE, respectively.

Most of the APE of the system is to be found in the first three baroclinic modes, accounting for 97.1% of the total APE. The barotropic mode accommodates no APE, but in

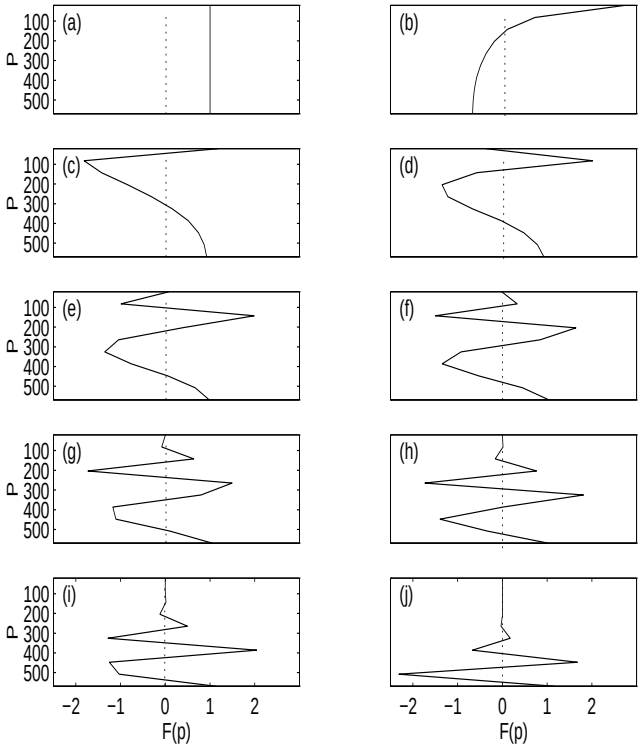

Fig. 6. Eigenmodes of the vertical structure equation for the stability profile shown in Fig. 1.

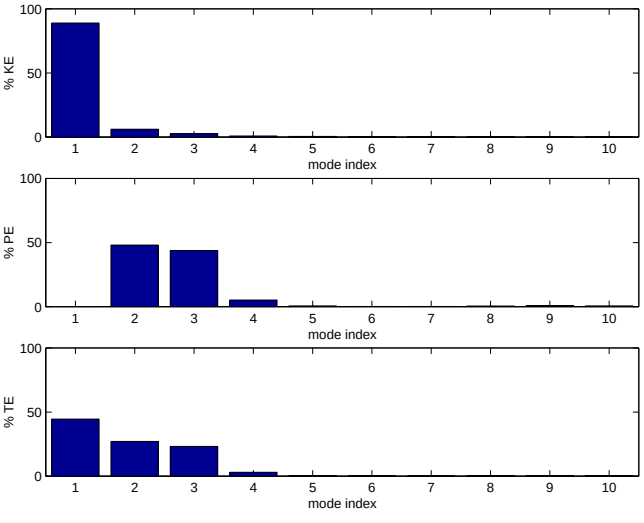

Fig. 7. Contributions to KE and PE from the barotropic (number 1) and baroclinic (remaining, numbers 2–9) modes.

the experiment analysed here, the first, second and third baroclinic eigenfunctions represent 48.1%, 43.9% and 5.1%, respectively of the total APE. Baroclinic modes 8 and 9 contain 0.89% and 0.64% of the total APE, respectively.

If modes 8 and 9 are neglected, the contribution of each successive mode to the TE is also a decreasing function of mode number, m. Additional numerical experiments in

Table 1. Table of Froude numbers of the associated vertical eigenmodes for the SGCM case.

Mode	Eigenvalue	Rossby radius of deformation	Froude number
Barotropic	$\lambda_0 = 0$	$Rd_0 = \infty$	0.0
Baroclinic 1	$\lambda_1 = 7.06 \times 10^{-7}$ km^{-2}	$Rd_1 = 1190.1$ km	8.14
Baroclinic 2	$\lambda_2 = 2.44 \times 10^{-6}$ km^{-2}	$Rd_2 = 640.2$ km	28.1
Baroclinic 3	$\lambda_3 = 6.21 \times 10^{-6}$ km^{-2}	$Rd_3 = 401.3$ km	71.5
Baroclinic 4	$\lambda_4 = 1.29 \times 10^{-5}$ km^{-2}	$Rd_4 = 278.4$ km	148.8
Baroclinic 5	$\lambda_5 = 2.29 \times 10^{-5}$ km^{-2}	$Rd_5 = 208.9$ km	263.7
Baroclinic 6	$\lambda_6 = 3.64 \times 10^{-5}$ km^{-2}	$Rd_6 = 165.7$ km	419.4
Baroclinic 7	$\lambda_7 = 5.37 \times 10^{-5}$ km^{-2}	$Rd_7 = 136.5$ km	618.4
Baroclinic 8	$\lambda_8 = 7.72 \times 10^{-5}$ km^{-2}	$Rd_8 = 113.8$ km	889.4
Baroclinic 9	$\lambda_9 = 1.21 \times 10^{-4}$ km^{-2}	$Rd_9 = 90.9$ km	1390.9

which the T21 spectral data were reduced to a T5 truncation also showed significant KE and APE contributions to be present in modes 8 and 9. Such modes may be an artifact of the vertical truncation level as well as consequences of the severe reduction in the vertical length scales. On the other hand, in the full Mars General Circulation Model (MGCM), and apparently in the Mars Global Surveyor/Thermal Emission Spectrometer (MGS/TES) observational analysis by Banfield et al. (2004), there are waves of different period (and sometimes wavenumber) that are trapped in very shallow layers near the surface. Also, since the data are derived from a primitive equation model, it is possible that activity with smaller vertical scales may not show up in the first few modes of a QG decomposition.

5 Various norms

We now address the question of which norm should be used to monitor energy conversion processes within the model, what emphasis each norm places on certain spatial and temporal structures within the data and how many patterns are required to reproduce the most "significant" dynamics of the model. In particular we shall investigate whether standard EOFs, which describe deviations from the mean state, should be used or whether the basis should describe the total state vector (and so include norms which maximise energy extractions).

We take as our basic state for the SGCM example, the steady state of the 2-D zonally symmetric version of the SGCM, obtained by suppressing the waves, after 400 sols (i.e. 400 Martian days), to ensure that the state has equilibrated (see also Collins, 1993). From the previous section, we see that it is necessary to retain the barotropic and at least the first two baroclinic modes in the vertical structure for our POD-Galerkin dimensional-reduction analysis. Appendix C describes the details of how PODs are calculated in practice in spectral space.

5.1 Projection of streamfunction or vorticity.

The question naturally arises regarding the choice between streamfunction and vorticity for the calculation of the POD modes (Selten, 1995). If vorticity is chosen, then the POD modes need to be optimised to describe the vorticity rather than the streamfunction, with the result that small-scale motions are emphasised (the inner product in this case defines enstrophy). We are, however, interested in large-scale circulations and so we shall use the streamfunction. It is important to note that the corresponding vorticity and planetary vorticity fields would not be described by the same set of PODs, and any resulting truncated POD model would not conserve both KE and enstrophy simultaneously. Furthermore, if forcing and dissipative terms are added, then neither KE nor enstrophy are conserved.

5.2 The KE and TE norms

The standard correlation norm gives

$$\mathbf{R}\Phi = \lambda\Phi, \tag{23}$$

where the covariance matrix $\mathbf{R}$ is defined by $R_{ij}=\overline{(V_i-\bar{V}_i)(V_j-\bar{V}_j)}$ with overbar denoting the time average. The POD modes, therefore, describe deviations from the mean state. Following Selten (1993), we can construct a set of basis functions which describe the total state vector, by replacing $\mathbf{R}$ by $\mathbf{C}$, where $C_{ij}=\overline{V_i V_j}$. The mean state is now retained in the POD expansion to allow for dynamical interactions between the mean background flow and the anomalous POD modes. The POD modes obtained using $\mathbf{R}$ optimise the variance whereas those obtained using $\mathbf{C}$ optimise the energy.

The inner product, defining the energy matrix $\mathbf{M}$, satisfies

$$< \mathbf{V}, \mathbf{V^T} >= \mathbf{V}^T\mathbf{M}\mathbf{V}, \tag{24}$$

so that the eigenvalue problem becomes

$$< \mathbf{V}, \mathbf{V}^T > \mathbf{M}^T\mathbf{U} = \lambda\mathbf{U}. \tag{25}$$

Since $\mathbf{M}$ is a diagonal matrix, $\mathbf{M}^T = \mathbf{M}$ and we obtain

$$\mathbf{C}\mathbf{M_p}\mathbf{U} = \lambda\mathbf{U}, \tag{26}$$

where the diagonal energy matrix $\mathbf{M}_p$ depends upon

$$< \psi, \psi >_p = \frac{1}{2}\int_0^{2\pi}\int_0^{\pi}\left(\nabla^p\psi \cdot \nabla^p\psi\right) a^2 \sin\theta d\theta d\phi, \tag{27}$$

for p=0, 1, 2, ..., and the basis $\mathbf{U}$ describes the total state vector.

5.3 Formation of the spectral energy matrix

The equality given in Eq. (9) for the KE yields:

$$\begin{aligned}\mathrm{KE} &= \frac{1}{2}\int_0^{\pi}\int_0^{2\pi}\sum_k \left[\nabla_h\widetilde{\psi}_k \cdot \nabla_h\widetilde{\psi}_k\right] a^2 \sin\theta d\theta d\phi \\ &= -\frac{1}{2}\sum_k \int_0^{\pi}\int_0^{2\pi}\left[\widetilde{\psi}_k \cdot \nabla_h^2\widetilde{\psi}_k\right] a^2 \sin\theta d\theta d\phi \\ &= \sum_{mnk} n(n+1)\widetilde{\psi}^2_{mnk},\end{aligned} \tag{28}$$

while Eq. (10) for the APE yields, for the TE:

$$\begin{aligned}\mathrm{TE} &= \mathrm{KE} + \frac{1}{2}\sum_k \int_0^{\pi}\int_0^{2\pi}\lambda_k\widetilde{\psi}_k^2\, a^2 \sin\theta d\theta d\phi \\ &= \mathrm{KE} + \sum_{mnk}\lambda_k\widetilde{\psi}^2_{mnk} \\ &= \sum_{mnk}\left(n(n+1) + \lambda_k\right)\widetilde{\psi}^2_{mnk},\end{aligned} \tag{29}$$

where $\widetilde{\psi}_k$ is the k-th baroclinic component in grid space and $\widetilde{\psi}_{mnk}$ is the coefficient at point (m, n) on the spectral grid of the k-th baroclinic component. Since these expressions must satisfy the inner product condition of Eq. (24), the spectral energy matrices take the form of the diagonal matrix discussed in Appendix D.

5.4 Comparisons between the SGCM Eigenspectra

Figures 8 and 9 show the eigenspectra (suitably normalised so that their sums equal unity) of the mean and perturbation fields computed using the correlation (labelled as I), KE (labelled as II) and TE (labelled as III) norms. From Fig. 8 we see that the first eigenvalue of the zonal flow dominates the spectra and captures 99.92% of the variance, 99.61% of the KE and 99.60% of the TE. The rate of decay of the eigenspectrum with respect to the correlation norm is faster for the zonal flow than with respect to the other two norms.

Figure 9 shows that the two leading eigenvalues of the perturbation flow represent 84% of the variance (in I), 79% of KE (in II) and 73% of TE (in III) if the correlation, KE or TE norms are used. Figure 9 shows that the first four wave modes appear in pairs. The dominance of these eigenmodes suggests that this flow in the original SGCM model could be governed by two wave pairs.

Table 2 gives an indication of how many eigenmodes would be required to capture 90% and 95% of the variance, KE and TE of the wave flow. Also given are the percentage of variance, KE and TE captured by 4, 10 and 50 eigenmodes. Only 5 correlation modes are required to capture 90% of the variance whereas 13 KE or 26 TE eigenvectors are needed if 90% of the KE or TE is to be retained. If an additional 5% of the variance, KE or TE is sought then an extra 9, 25 or 30, respectively of correlation, KE and TE eigenvectors are required.

A sudden decrease from large to small eigenvalues with increasing EOF index (as in the correlation norm), offers a natural criterion for selecting how many patterns are required to describe the flow. Figure 9, for example, shows a sudden decrease by a factor of 100 exists beyond wave pattern 2. Therefore only two modes would suffice to describe the model dynamics to a first approximation (see also Kantz and Schreiber, 1997).

5.5 SGCM POD modes

Figure 10 illustrates the horizontal structure of the barotropic components of the various POD eigenmodes computed with the correlation norm. Here modes 1 and 2 represent a steady wavenumber 3 in the southern hemisphere, which are $\frac{\pi}{2}$ out of phase. Modes 3 and 4 correspond to a steady wavenumber 2 and mode 5 depicts a mean zonal flow. Also evident is a wavenumber 6 structure in modes 6, 8 and 10. Figure 10 illustrates that modes 1 and 2, 3 and 4 form conjugate pairs. However, the choice of norm affects the ordering of these modes.

Figures 11–16 show the barotropic and baroclinic components of the SGCM POD wave modes with respect to the three different norms.

Modes 1 and 2 form a conjugate pair for each of the norms and so denote a travelling wavenumber 3 in the longitudinal direction. The structure of mode 1 is unaffected by the choice of norm (see Figs. 11, 13 and 15) and contains a strong wavenumber 3 component centred at a latitude of about 45° S. The barotropic components are almost sinusoidal in longitude. The first baroclinic components comprise two parallel wavenumber 3 structures, centred at latitudes of 45° S and 15° S, respectively, displaced by 50° in longitude. There are additional wavenumber 3 patterns, centred at 20° N in the northern hemisphere (NH). The second baroclinic mode also contains similar parallel wavenumber 3 patterns, centred at latitudes of 45° S and 25° S, displaced by 25° in longitude with a strong wavenumber 3 structure at 20° N. The third baroclinic mode is almost symmetrical about the equator but tilted in the SH. A sinusoidal wavenumber 3 pattern exists at 20° N, together with two wavenumber 3 patterns at latitudes of 15° S and 50° S, where the latter wave pattern is displaced by 50° in longitude.

Mode 3, in Figs. 11, 13 and 15, contains a strong wavenumber 2 pattern in each vertical component. With the correlation or the KE norm, the barotropic component appears to be nearly sinusoidal but somewhat distorted with the TE norm. Similarly, the first and second baroclinic components of the correlation and KE modes contain a latitudinally

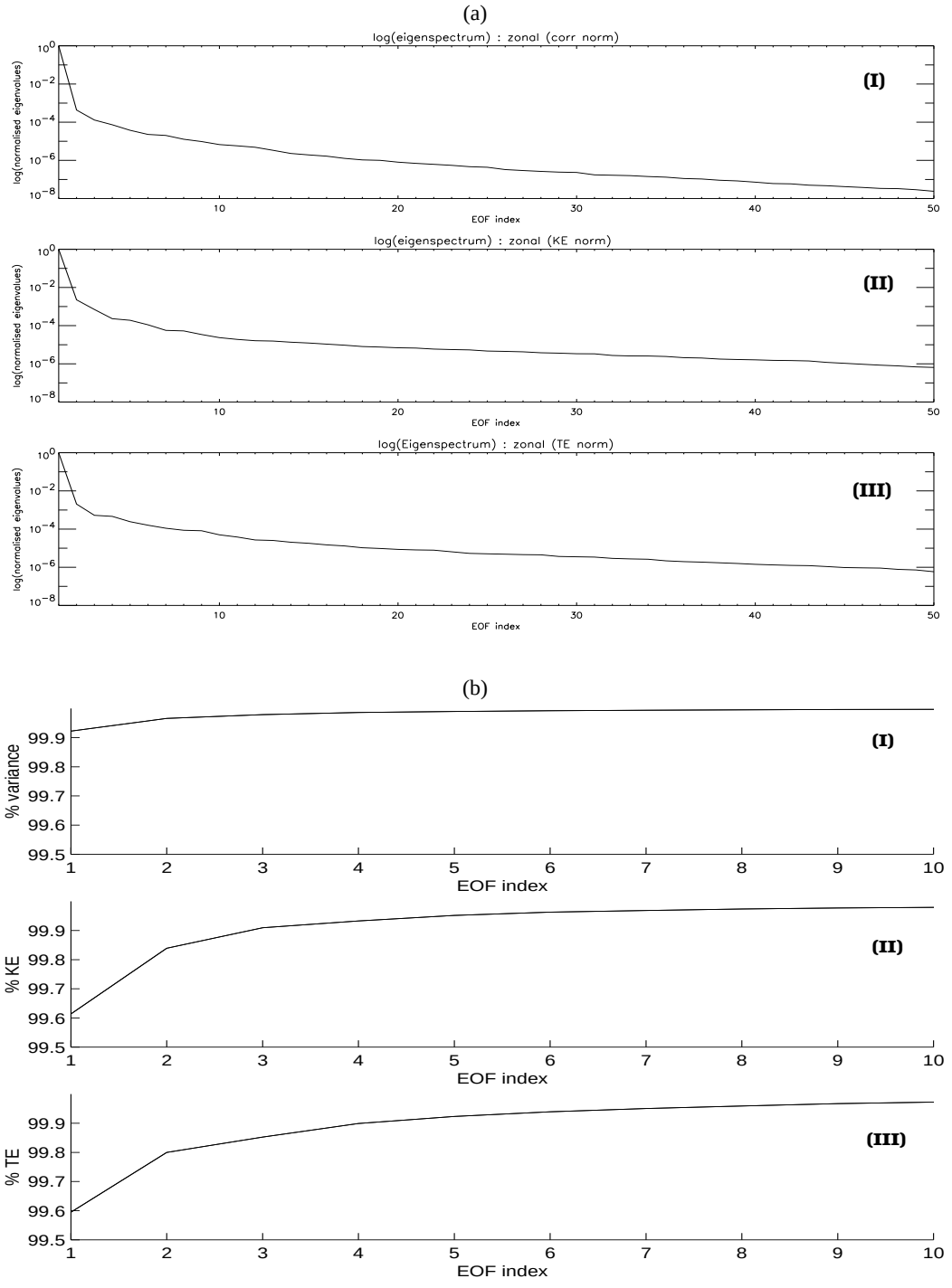

Fig. 8. (a) The logarithmic eigenspectra zonal profiles using the (I) correlation, (II) KE and (III) TE norms. **(b)** The cumulative variance (I), KE (II) and TE (III) capture of the zonal field using the correlation (I), KE (II) and TE (III) norms, respectively.

stretched wavenumber 2 pattern, together with a small wave 3 structure centred at a latitude of 20° N, which is displaced by 100° in longitude. However in the TE case, this mode contains a severely modulated wave 2 structure, centred at 25° in the SH. The third baroclinic components produce very similar structures in both the correlation and KE norms: both are centred at latitudes of ±45°, with a thin band of distortion about the equator (giving rise, very nearly, to a wave 3 on the equator). The TE norm, however, produces a sinusoidal wavenumber 6 pattern at 25° S. Clearly, correlation modes 3 and 4 form a conjugate pair, whereas it is modes 3 and 5 in the energy norms. The correlation mode 5 describes a departure from the mean flow, suggesting that the choice of norm significantly effects the ordering of the modes.

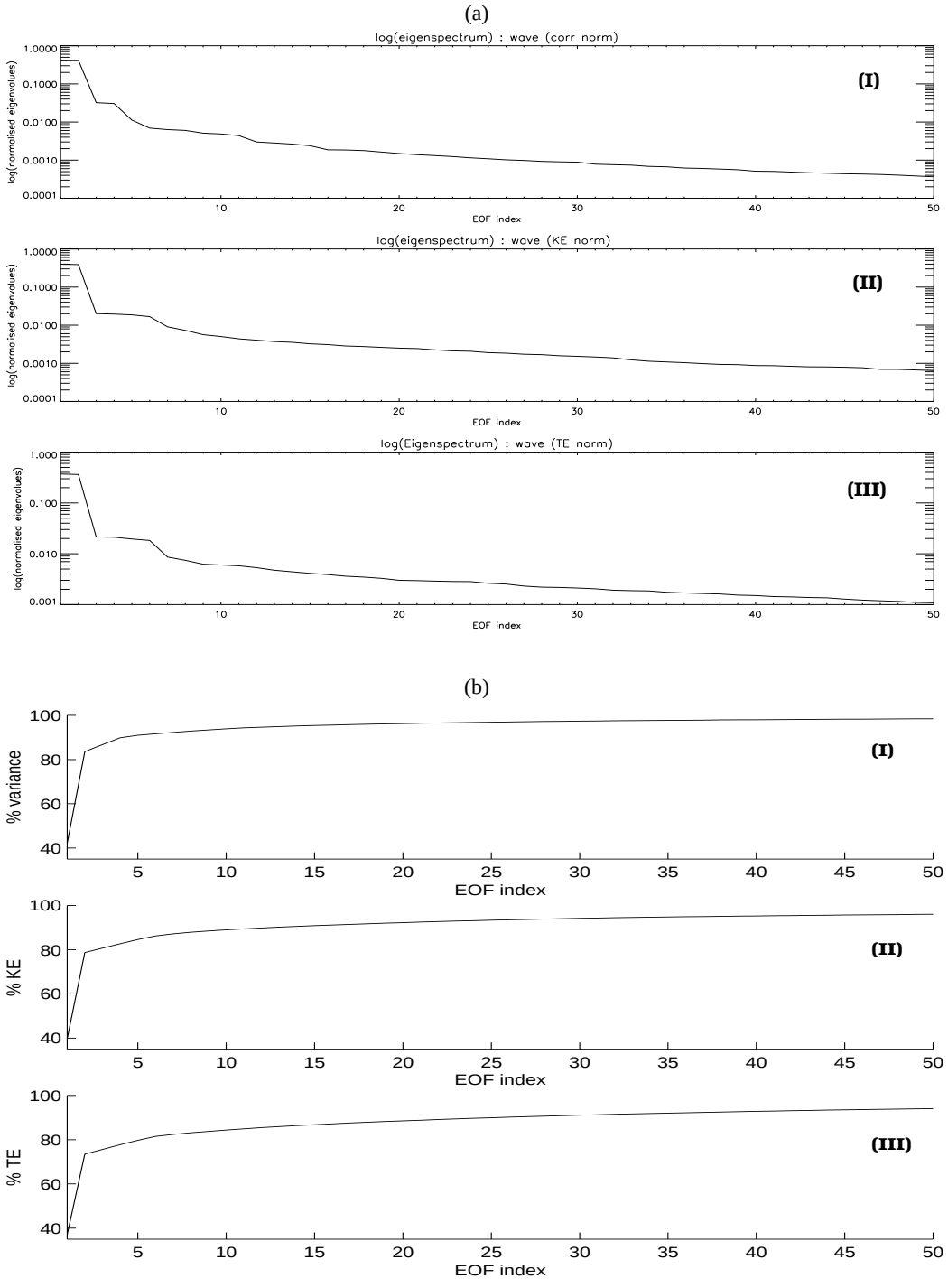

Fig. 9. As Fig. 8, but for the departure fields.

Table 2. POD modal truncation against variance/energy capture in the departure flow.

Norm	90 %	95 %	4 modes	10 modes	50 modes
Correlation	5 modes	14 modes	89.83 %	93.88 %	98.44 %
KE	13 modes	38 modes	82.68 %	88.94 %	96.01 %
TE	26 modes	56 modes	77.72 %	84.34 %	94.07 %

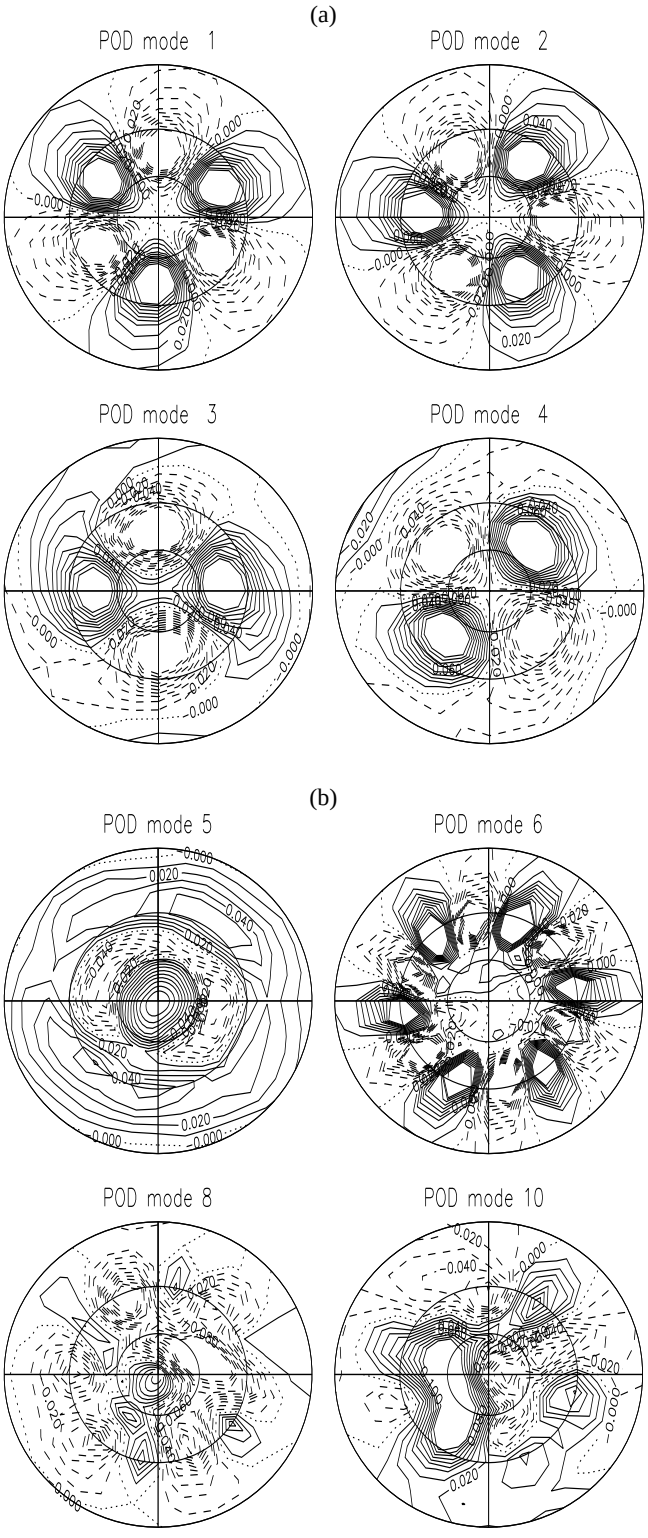

Fig. 10. Southern hemisphere stereographic projection plots of **(a)** the first four SGCM POD modes of the barotropic component and **(b)** modes 5, 6, 8 and 10, obtained using the correlation norm.

Table 3. Zonal wavenumbers associated with each of the POD modes (wavenumber 0 is zonal-mean flow).

Modes	Correlation	KE	TE
1	3	3	3
2	3	3	3
3	2	2	2
4	2	6	6
5	0	2	2
6	6	6	6
7	4	4	4
8	6	4	4
9	4	3	4
10	4	3	4

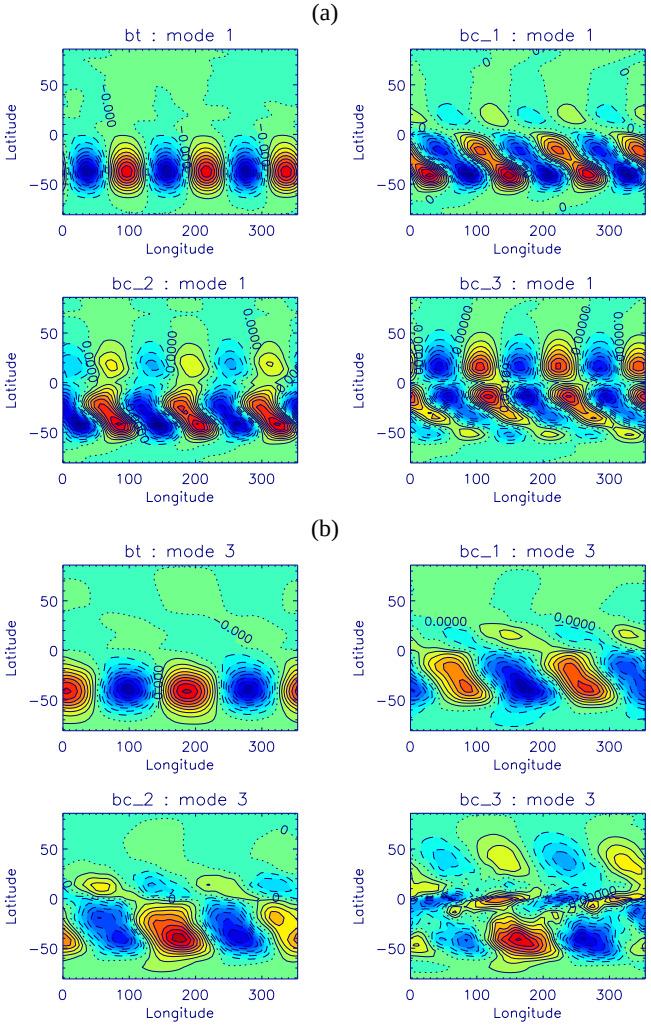

Fig. 11. The barotropic (bt) and three leading baroclinic components (bc_1, bc_2 and bc_3) of the SGCM POD modes 1 **(a)** and 3 **(b)** using the correlation norm. In this and following colour figures, positive values are shaded red and negative, blue, with zero lying in mid-green.

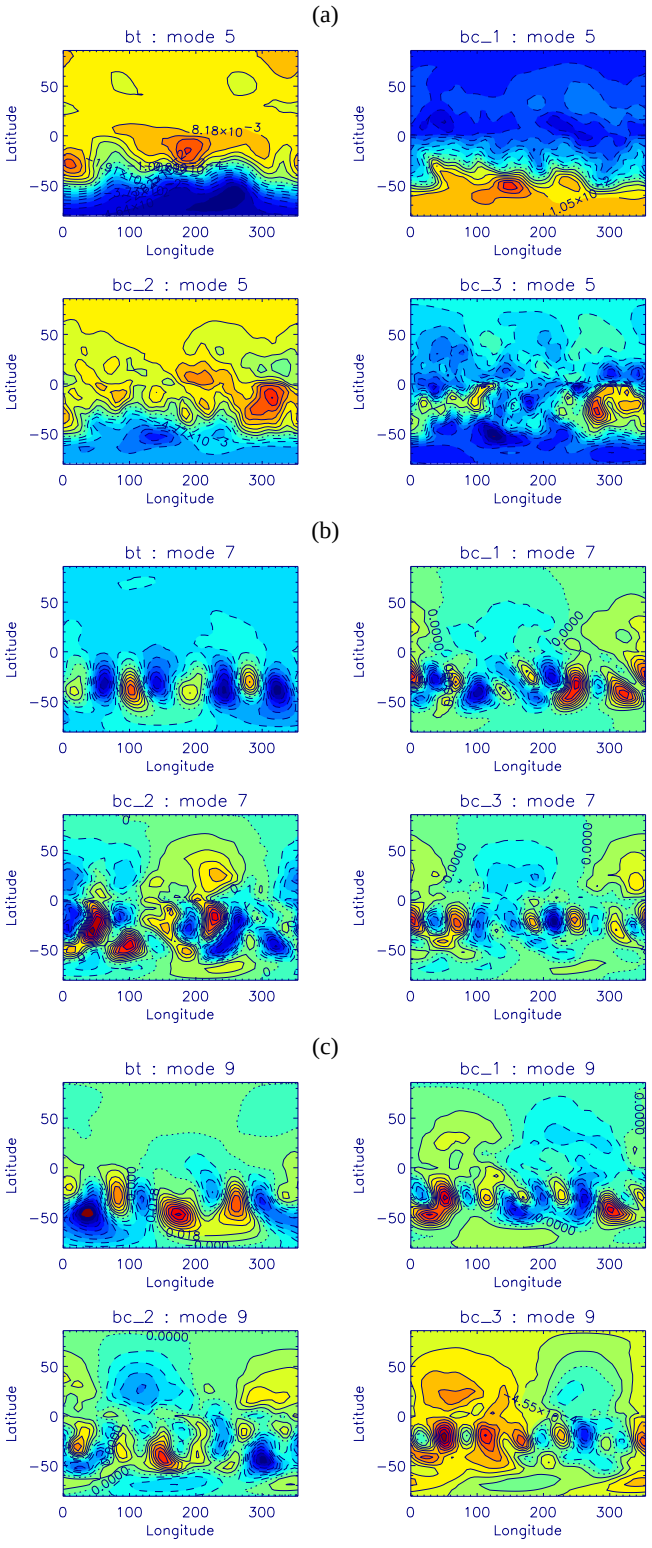

Fig. 12. The barotropic (bt) and leading three baroclinic components (bc_1, bc_2 and bc_3) of modes 5 **(a)**, 7 **(b)** and 9 **(c)** using the correlation norm.

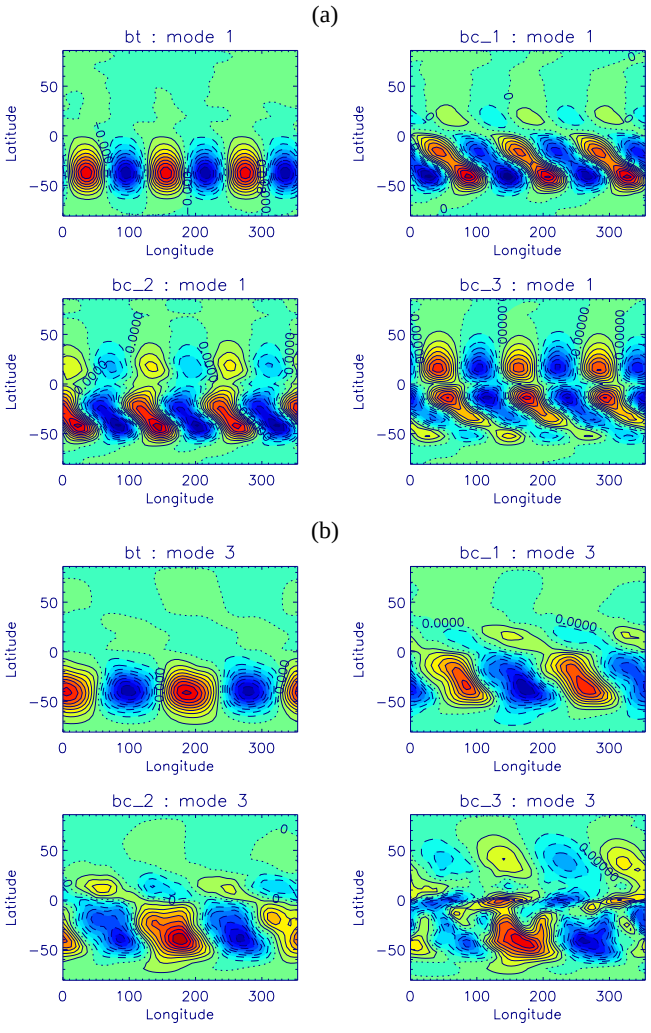

Fig. 13. The barotropic (bt) and leading three baroclinic components (bc_1, bc_2 and bc_3) of modes 1 **(a)** and 3 **(b)** using the KE norm.

Mode 7 has a wave 4 structure (see Figs. 12, 14 and 16), which is almost sinusoidal with the energy norms but more complicated with the correlation norm. The barotropic component for each norm has a wavenumber 4 structure, centred at 35° in the SH. The first baroclinic components contain two parallel wave 4 structures, centred at 45° and 15° in the SH, and displaced by 25° in longitude in the correlation norm case, while for the energy norms, the modes are more regular in structure. The second baroclinic components also contain two parallel wave 4 structures, but now centred at 50° and 25° in the SH with a large wavenumber 1 component in the NH, at 30°. The third baroclinic component of the KE and TE mode 7 give structures similar to the first baroclinic component. Both energy 8 modes contain dominant zonal wavenumber 4 structures whereas the correlation norm mode 8 contains wavenumber 6 structures.

The correlation norm generates wavenumber 4 patterns in the barotropic and first baroclinic components of mode 9, although the second and third baroclinic components contain wave 6 structures at a latitude of 25° in the SH. The barotropic component of KE mode 9 contains two parallel wavenumber 3 structures centred at 50° and 25° in the SH,

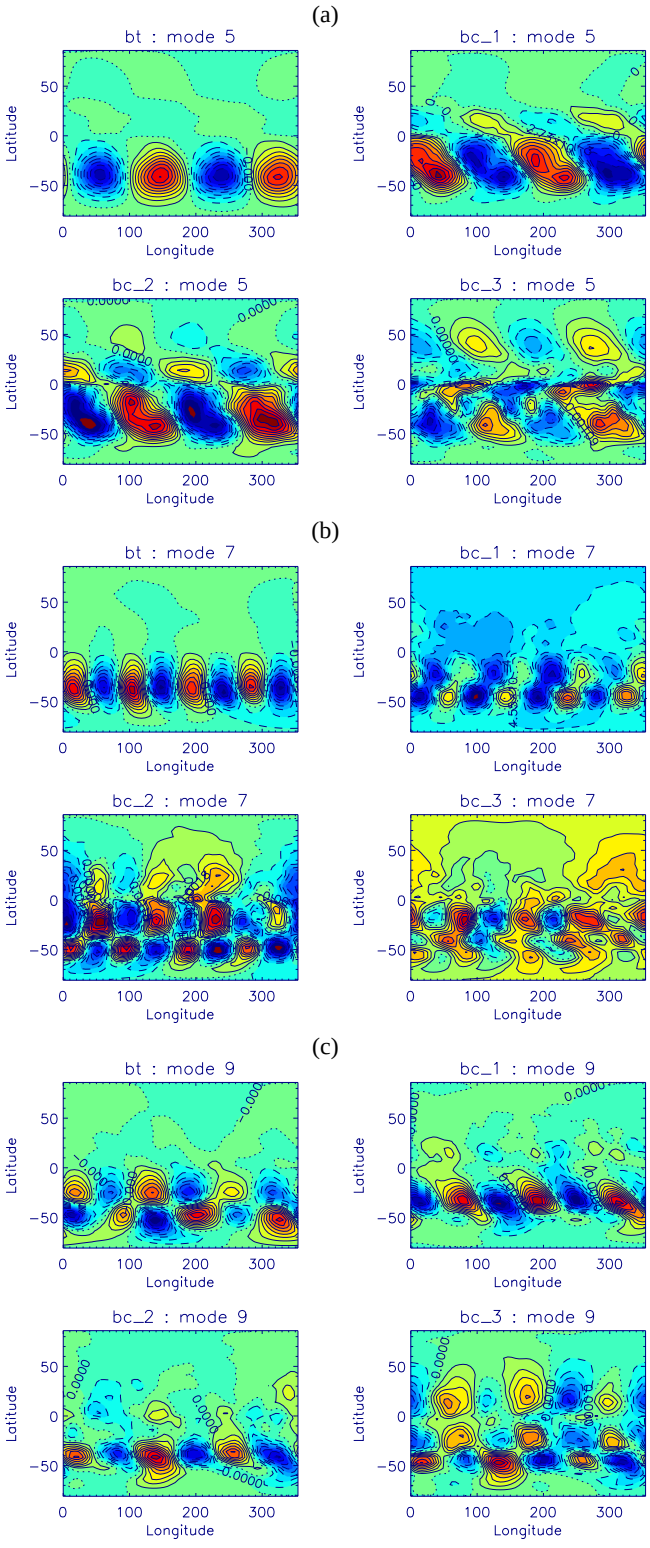

Fig. 14. The barotropic (bt) and leading three baroclinic components (bc_1, bc_2 and bc_3) of modes 5 **(a)**, 7 **(b)** and 9 **(c)** using the KE norm.

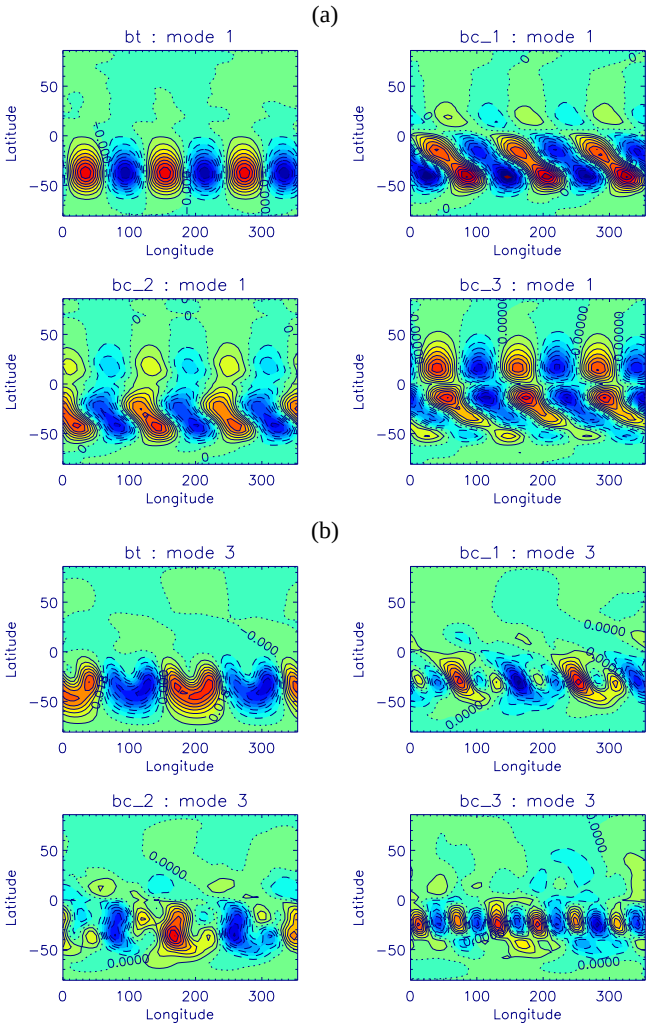

Fig. 15. The barotropic (bt) and leading three baroclinic components (bc_1, bc_2 and bc_3) of modes 1 **(a)** and 3 **(b)** using the TE norm.

displaced by 50° in longitude. However the TE norm has a wave 4 at 45° in the SH. The first baroclinic components of KE and TE modes 9 are tilted wavenumber 3 patterns, centred at 35° in the SH, with an additional wave 3 at a latitude of 20° in the NH and displaced by 25° in longitude. The energy norms produce wavenumber 3 patterns in the second baroclinic component, at latitudes of 45° in the SH and on the equator, displaced by 15° in longitude. The third baroclinic component of the energy modes contain three wave 3 patterns at latitudes of 50° and 25° in the SH and 20° in the NH.

Thus modes 1 and 2 for each of the norms form a complex conjugate pair and depict a travelling wavenumber three, whereas modes 3 and 4 for the correlation norm and modes 3 and 5 for the energy norms depict a travelling wavenumber 2 structure. Hence two distinct travelling waves can be observed from the leading order POD modes. The different norms also rearrange the ordering of the spatial eigenmodes.

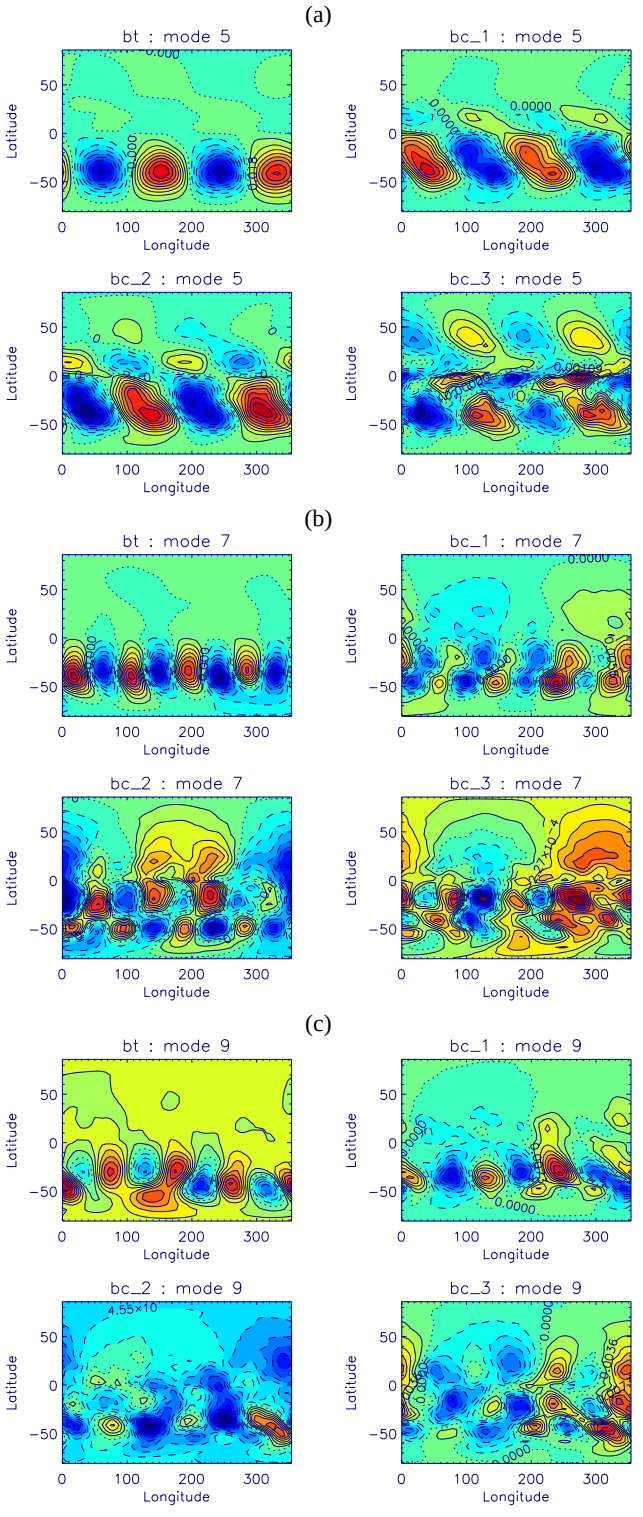

Fig. 16. The barotropic (bt) and leading three baroclinic components (bc_1, bc_2 and bc_3) of modes 5 **(a)**, 7 **(b)** and 9 **(c)** using the TE norm.

5.6 SGCM Principal Components

The Principal Components (PCs) represent the time-varying amplitudes of the POD eigenvectors at a given time. Specifically if $\mathbf{x}_j$ is part of the time series of one of the dependent variables, then

$$\mathbf{x}_j = \sum_{i=1}^{m} a_{ij}\mathbf{V}_i, \tag{30}$$

where a_{ij} is the PC of the i-th eigenvector $\mathbf{V}_i$ in the expansion of $\mathbf{x}_j$. When the eigenvectors form an oscillating pair, the square root of the sum of the squares of the two PCs (in the L^2 norm) represent the amplitude of the oscillation at any given time.

Figure 17 shows the temporal behaviour of the perturbation spatial eigenmodes for the three different norms over 300 Martian days (sols).

The structures are wave-like, with the two leading PCs being wavenumber 3 structures, one quarter of a period out of phase, oscillating with a period close to 0.23 cycles/sol. The form of these two PCs is virtually unaffected by the choice of norm. The higher order PCs appear to vary more irregularly in time, particularly PCs 6 to 10 where high frequency structures can be observed. Recall that the ordering of the spatial POD modes is affected by the choice of norm, and so comparisons between the various PCs must take this into account.

PCs 3-5 display a long time modulation, as well as a short time variability. The correlation norm PCs 3 and 4, and the energy norms PCs 3 and 5, form complex conjugate pairs, and so represent travelling waves. The travelling wavenumber 2 structures oscillate at a rate of about once every 12 days, giving a frequency of about 0.08 cycles/sol. This is consistent with the frequency values picked out by the power spectral analysis in Fig. 18a where peaks are clustered about the 0.08–0.1 cycles/sol frequency band.

The correlation and TE norms extract similar wave patterns in PC 4, as is visible in the clustering of peaks about 0.1 cycles/sol. This is interesting since the spatial patterns associated with POD mode 4 are very different. The correlation norm mode contains a wavenumber 2 structure, while the KE and TE norm modes have a wavenumber 6 structure. However, the wavenumber 6 structure in the KE case has a very different temporal behaviour to that of the correlation and TE norms. Its 4th PC has a much higher frequency dependence, small in amplitude and fluctuating about zero with a cluster of frequencies about 0.5 cycles/sol.

KE and TE PCs 3 and 5 form complex conjugate pairs and so describe a travelling wave. This is apparent by comparing the power spectra of PC 3 in Fig. 18a with that for PC 5, shown in Fig. 18b. The energy norms produce structures with a dominant frequency of about 0.1 cycles/sol, whereas the correlation POD mode 5, which represents a departure from the mean flow, has a small amplitude temporal behaviour with a very low frequency of about 0.006 cycles/sol.

Since the temporal evolution of PCs 6 to 10 are far more complicated and irregular than the leading five PCs, the power spectra in Fig. 18b reveal a much broader range of interacting frequencies in their power spectra.

Figure 19 shows the time dependence of the mean-flow correction modes. We again find that PC 1 is almost insen-

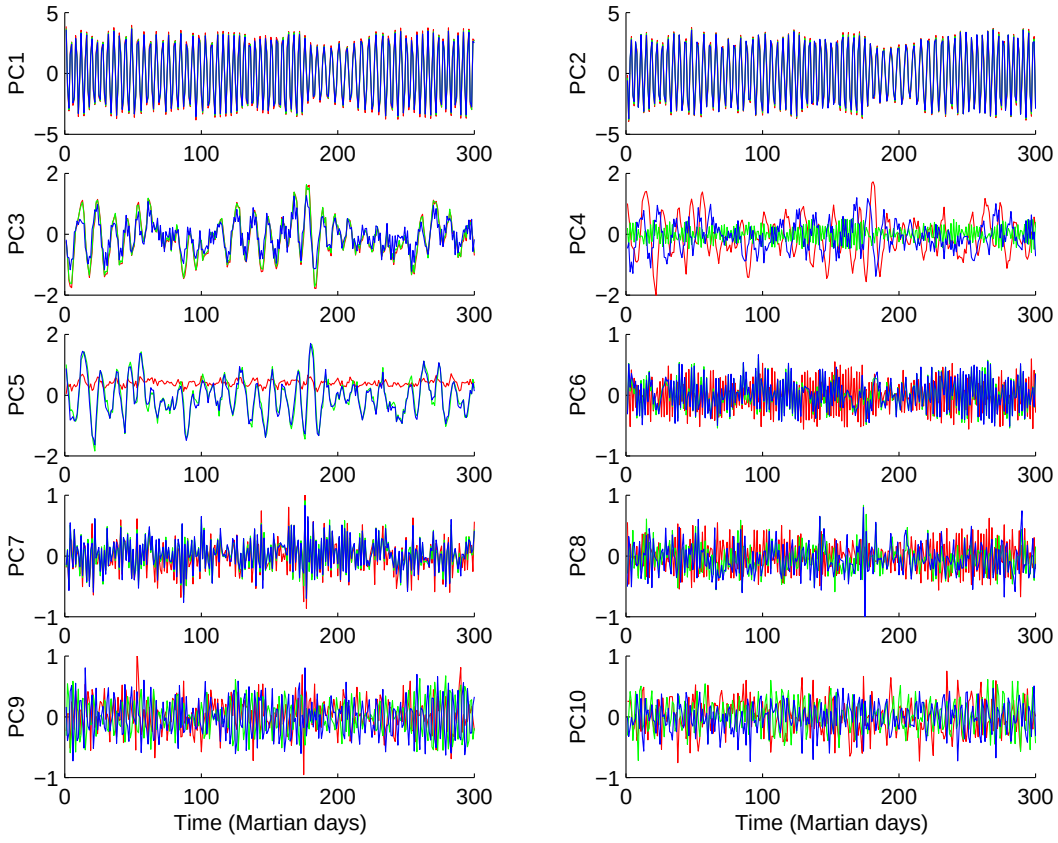

Fig. 17. Original SGCM departure principal components (PCs) using the correlation (red), the KE (green) and the TE norms (blue) shown during an interval of 300 Martian days. Note that the range of PC1 and PC2 is five times, and that of PC3–5 is twice, that of the higher order modes PC6–10.

sitive to the choice of norm, whereas PCs 2 to 10 contain strikingly different oscillatory behaviour. One reason might be due to almost all of the TE of the flow being contained in the zonal mean (in excess of 90%). Since the APE in the zonal flow accounts for almost 50% of the TE, maximisation of KE or TE produces significant differences in the spatial and temporal patterns.

As the leading travelling waves propagate at a frequency of about 0.23 cycles/sol (i.e. the spatial wave three mode) and 0.08 cycles/sol (i.e. the spatial wave two mode), it might then be a reasonable hypothesis that such behaviour could be emulated with a low-dimensional model. Since the analysis picks out two frequencies of oscillation, there could be some degree of weak interaction occurring between the leading order spatial modes, suggesting how crucial it is to retain a 'sufficient' amount of information regarding the behaviour of the two travelling spatial wave patterns. Thus for this particular data set, the highly regular baroclinic wave activity in the idealised Martian atmosphere is nearly bimodal.

5.7 Energy in the SGCM eigenmodes

We conclude with a discussion of the energy distribution between the various individual POD modes.

The streamfunction data was decomposed into a basic-state, mean-flow correction (MFC) and a wave flow. The zonal flow, defined as basic state + MFC, accounts for 97.85% of the total variance, 90.73% of KE and 93.68% of TE if the correlation, KE and TE norms respectively are used.

Figure 20a shows histograms of KE as a fraction of TE in the zonal POD modes using the (I) KE and (II) TE eigenvectors. Modes derived using the TE norm extract the APE of the original system far more efficiently than with the KE norm. Since Fig. 7 showed that leading zonal mode accounts for over 90% of the total energy in the system, the amount of KE and APE captured will almost be equal to the total KE and APE contained in the truncated system. Figure 20a shows that 59% of the TE in the first zonal eigenmode is in the form of KE with the KE norm, indicating that this has inefficiently captured the SGCM APE. This is consistent with the fact that the KE norm optimises KE and not APE. With respect to the TE norm, 48% of the TE in the leading zonal mode is in the form of KE and so the original balance between KE and APE has been retained.

The KE norm also concentrates a large proportion of the system's KE into the leading order modes. This contrasts with the TE eigenmodes which contain a very significant proportion of KE in the higher-order modes (about 80%), and

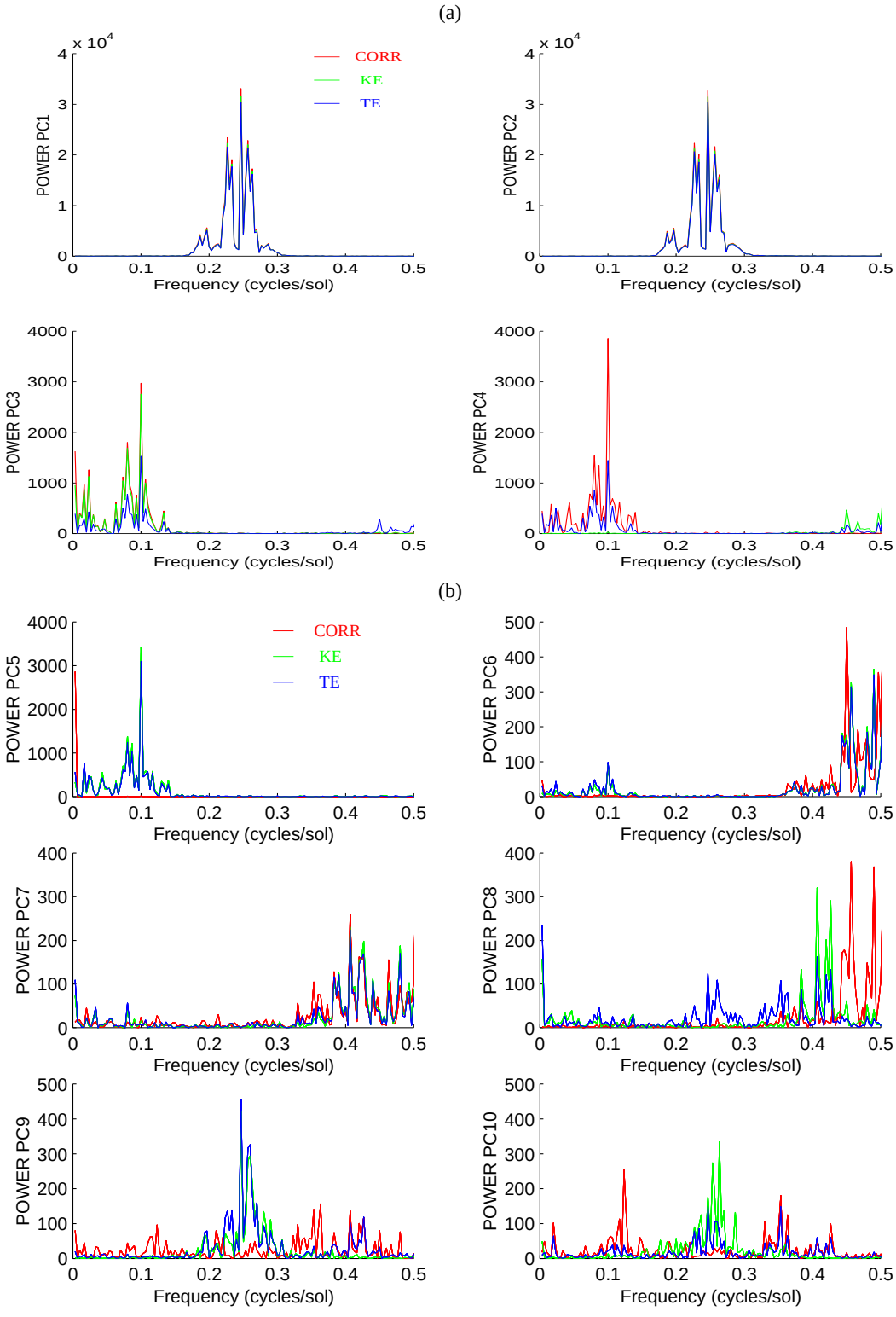

Fig. 18. Power spectra profiles of the original SGCM departure PCs where **(a)** shows the frequencies of PCs 1 to 4 and **(b)** shows the frequencies of modes 5 to 10 using the correlation (red), KE (green) and TE (blue) norms.

suggests that the TE eigenvectors have placed most of the APE in the leading order modes and so have effectively optimised the capture of APE.

Figure 20b shows KE as a fraction of TE in the wave field POD modes using the (I) KE and (II) TE eigenvectors. The leading KE modes account for about 70% of TE, but after

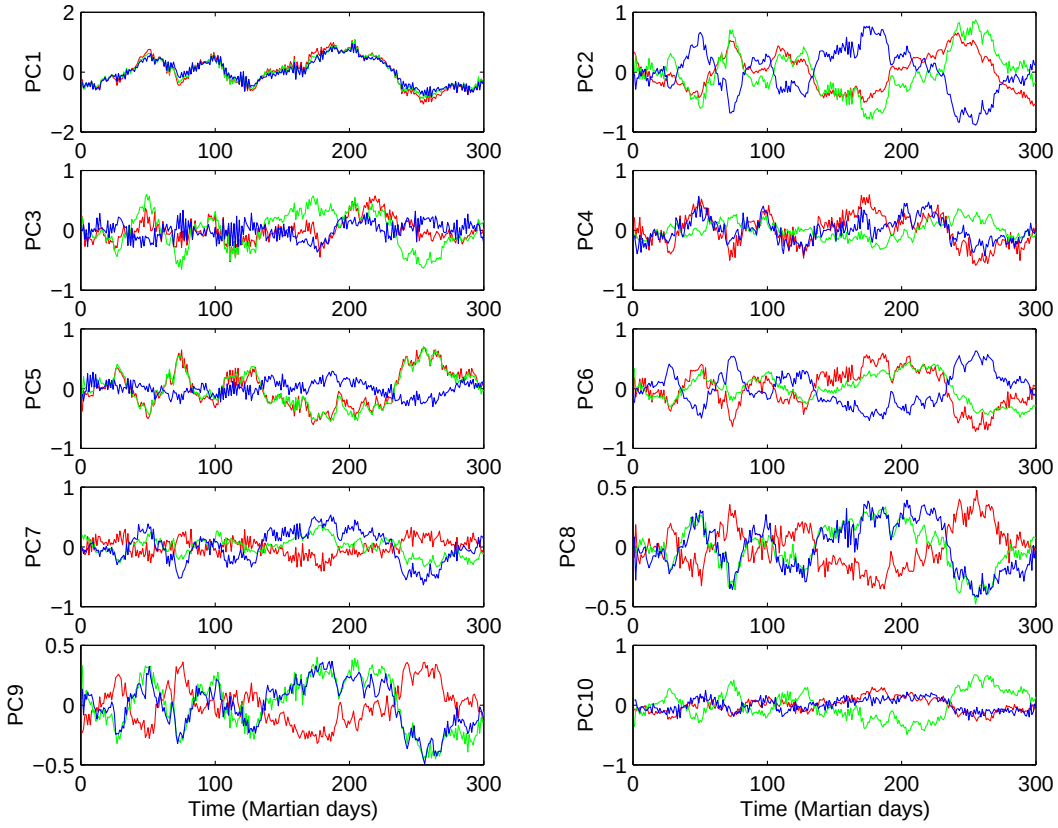

Fig. 19. Original SGCM principal components (PCs) of the mean-flow correction field using the correlation (red), the KE (green) and the TE norms (blue) during an interval of 300 Martian days.

14 KE eigenvectors there is a steep decay in the KE profile, implying that the low-order TE modes capture most of the APE. However, the higher-order TE eigenvectors contain mainly KE, which again indicates that the KE norm places the majority of its KE into the leading order modes, whereas the TE norm pushes the APE into the lower-order modes.

These results agree with Selten (1993), who found that, for the Earth, eigenvectors obtained with different norms behave differently in terms of how much KE and APE was captured by each mode. He also showed that the KE norm distributed the majority of the KE into the leading order modes, whereas the higher-order eigenvectors were dominated by APE. In contrast, the TE norm placed most of the APE in the leading order eigenmodes, leaving a greater fraction of KE in the higher-order modes.

6 Discussion

The model has been shown to do remarkably well at capturing a signficant fraction of the total energy and/or variance, using a relatively small number of vertical and horizontal modes. When just four vertical modes (the barotropic and first three baroclinic modes) are retained in the reduced-order approximation, the correlation norm captures approximately 90% of the variance, while the kinetic energy and total energy norms capture approximately 83% and 78% of the kinetic and total energy respectively.

The degree of dimensional reduction achieved here is notable, from $O(10^4)$ degrees of freedom in the primitive equation SGCM to $O(50)$ total modes in the reduced dimension model. Baroclinic waves on Mars appear to be more regular than those on Earth (Read and Lewis, 2004) and this may account for the relative success of the present Martian reduced order model. Recent investigations of low-order models for the Earth's atmosphere suggest that many more modes, at least 500, are required to account for 90% of the variance in terrestrial models (Achatz and Branstator, 1999; Achatz and Opsteegh, 2003a,b), although it might be possible to reproduce aspects of low-frequency variability in a low-resolution quasi-geostrophic model using $O(10)$ modes (D'Andrea and Vautard, 2001; D'Andrea, 2002).

In a more realistic model of the Martian atmosphere, which includes diurnal and seasonal thermal forcing cycles, topography and planetary boundary layer effects, for example, both the vertical and horizontal modal spectra are likely to be significantly richer in structure (Martinez-Alvarado et al., in preparation).

In part 2 we will develop a hierarchy of POD-Galerkin modal truncations, using both two and four vertical modes with the correlation, kinetic energy and total energy norms, as a prelude to performing a bifurcation analysis and a com-

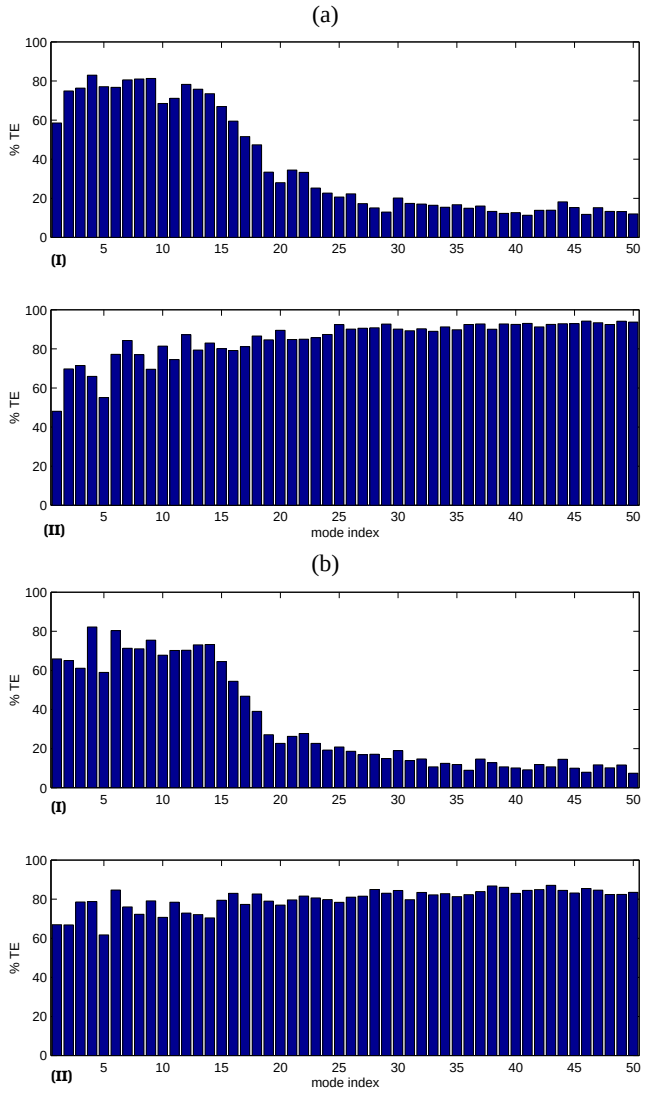

Fig. 20. KE as a fraction of TE contained in (a) the zonal modes and (b) the wave modes for the (I) KE and (II) TE eigenvectors.

parison with the full SGCM integration.

Appendix A The numerical scheme

We solved Eq. (5) numerically using finite differences for a given profile of the stratification parameter $S(\sigma)$, derived from the SGCM:

$$\frac{\partial}{\partial\sigma}\frac{{f_0}^2}{S_i}\frac{\partial}{\partial\sigma}H_i \sim \frac{{f_0}^2}{S_{i+1}(\delta\sigma_{i+1})^2}(H_{i+1}-H_i) - \frac{{f_0}^2}{S_i(\delta\sigma_i)^2}(H_i-H_{i-1}). \quad \text{(A1)}$$

Taking $\delta\sigma_i{=}K$ for some constant $K{\in}\mathbb{R}$, results in the vertical modal problem being solved over equally-spaced sigma levels (see Sect. 4), so that

$$\frac{{f_0}^2}{S_iK^2}H_{i-1} - \frac{{f_0}^2}{K^2}\left(\frac{1}{S_i}+\frac{1}{S_{i+1}}\right)H_i + \frac{{f_0}^2}{S_{i+1}K^2}H_{i+1} + \lambda H_i = 0. \quad \text{(A2)}$$

This yields an eigenvalue problem $\mathbf{C}\mathbf{H}_k{=}\lambda_k\mathbf{H}_k$, where $\mathbf{C}$ is a symmetric, tridiagonal matrix and vector $\mathbf{H}_k{=}(H_k(\sigma_1), ..., H_k(\sigma_N))$, where we chose $N{=}10$ as in the SGCM experiments of Collins and James (1995). The boundary conditions were chosen to be $d\mathbf{H}/d\sigma{=}0$ at $\sigma{=}\sigma_1$ and $\sigma{=}\sigma_N$ (and were implicitly satisfied in Eq. (A1) by specifying $S_1{=}S_{N+1}{=}\infty$).

The numerical code for Eq. (A2) was verified by setting the stratification parameter $S(\sigma)$ to be constant in the vertical structure equation; as expected, sine and cosine functions were obtained as the eigenfunctions H_i.

In the SGCM, we took the following: $p{=}p_0{+}p'$ is pressure where $p_0{=}610\,P_a$ is the basic term and p' is the perturbation; $T{=}T_0{+}T'$ where $T_0{=}200\,\mathrm{K}$; $R{=}191.2\,\mathrm{JKg^{-1}\,K^{-1}}$ is the gas constant for dry air; $\Omega{=}7.08822{\times}10^{-5}\,\mathrm{s^{-1}}$ is the rotational rate of Mars; $a{=}3.394{\times}10^6\,\mathrm{m}$ is the radius of the planet.

Appendix B The spectral grid

Since the streamfunction data lies on a jagged T21 spectral grid, it is useful to explain the ordering of the spectral coefficients on such a grid.

The order of data storage is by level, beginning at the top level where $\sigma{=}0.05$. For each level there are odd and even complex coefficients (odd for a cosine and even for a sine coefficient), with an equal number of odd and even coefficients. If n is the total wavenumber and m the zonal wavenumber (so that there are $n{-}|m|$ zeros between the north and south poles), the ordering of the coefficients is similar to that shown in Fig. 5.1 for the $T5$ and $T4$ truncations. The coefficients are read in order of increasing n with increasing m, beginning with the even and then the odd coefficients (for full details see Blackburn, 1985).

Specifically, if A_n^m is the spectral coefficient at position (n, m) on a spectral grid, then the coefficients are read in the following order:

EVEN $A_0^0, A_2^0, A_4^0, ..., A_1^1, A_3^1, ..., A_2^2, A_4^2, ..., A_{NN-1}^{NN-1}$,

ODD $A_1^0, A_3^0, A_5^0, ..., A_2^1, A_4^1, ..., A_3^2, A_5^2, ..., A_{NN-1}^{NN-1}$,

where NN is the highest total wavenumber retained in the spectral series.

D_i^E are the diagonal matrices for the even spectral entries of the i-th baroclinic component (recall $i{=}0$ is the barotropic and $i{=}1, 2, 3$ are the first three baroclinic modes), while D_i^O are the analagous blocks for the odd entries.

The diagonal blocks of the even spectral entries for the KE and TE matrices are

KE $\mathbf{D}_i^E = \mathbf{diag}\,[n_1(n_1+1),$

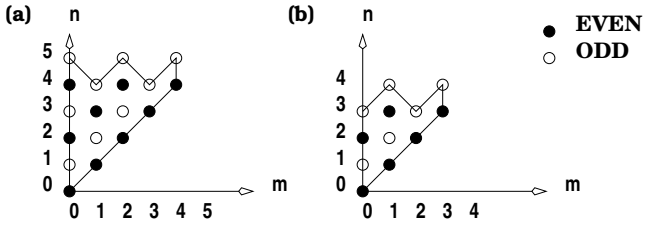

Fig. B1. The spectral grids for a jagged **(a)** T5 and **(b)** T4 triangular truncations. Coefficients are read in order of increasing n (total wavenumber) with increasing m (zonal wavenumber) for the even then the odd coefficients.

$$\boxed{\text{TE}} \quad \mathbf{D}_i^E = \mathbf{diag}\big[n_1(n_1+1)+\bar{\lambda}_i, \; n_2(n_2+1), \ldots, n_s(n_s+1)], \; n_2(n_2+1)+\bar{\lambda}_i, \ldots, n_s(n_s+1)+\bar{\lambda}_i\big],$$

where n_i is total wavenumber of the i-th even spectral coefficient, the subscript s={$n(m$+1)+max$(m, n)+1$}/2, and coefficients are read in order of increasing n with increasing m as shown in Fig. B1.
Finally $\bar{\lambda}_i$ corresponds to the i-th Froude number obtained from the vertical structure equation in Sect. 3 above.

Appendix C Calculation of PODs in spectral space

Although POD modes are usually calculated in physical grid space, we have found it to be more computational efficient to perform this calculation in spectral space (see e.g. Schubert, 1985; Selten, 1995). Both methods are related via a linear transformation. Because the data is truncated spectrally at T21, the POD modes also retain all wavenumbers up to a total wavenumber 21. In grid space, a covariance matrix of at least $(48\times24)^2$ would be required for a T21 spectral resolution (the SGCM actually transforms to a 64×32 real space grid, using fast transform techniques, oversampling in order to limit wave aliasing from nonlinear products during integration; using this grid data directly would imply a covariance matrix of size 9,437,184), whereas a T21 data set can be fully resolved with 242 real odd and even spectral data points, yielding a spectral covariance matrix of size 484,484 for the same resolution. We used the NAG routine F02ABF to calculate the eigenvalues and eigenvectors of the resulting real symmetric matrix. The computational speed of this calculation scales like l^3 (where l is the order of the matrix), so that the spectral problem runs approximately $(4.23)^3$ times faster than an equivalent grid space formulation.

If the covariance of the streamfunction is defined as

$$C(\theta,\phi,\theta',\phi') = r^2\sqrt{\sin\theta\sin\theta'}\left(\overline{\psi(\theta,\phi)\psi(\theta',\phi')}\right), \quad \text{(C1)}$$

where the overbar denotes a time average, then the eigenvalue problem on a sphere becomes:

$$\frac{1}{2\pi^2}\int_0^{2\pi}\int_0^{\pi} C(\theta,\phi,\theta',\phi')\Upsilon_i(\theta',\phi')d\theta'd\phi' = \lambda_i\Upsilon_i(\theta,\phi), \quad \text{(C2)}$$

where $\Phi_i(\theta,\phi)=\Upsilon_i(\theta,\phi)/\sqrt{\sin\theta}$ is the i-th POD mode.

Expanding both the streamfunction $\psi(\theta,\phi,t)$ and the spatial eigenmodes $\Phi_i(\theta,\phi)$ as a jagged T21 spectral truncation, we have:

$$\psi(\theta,\phi,t) = \sum_{m=0}^{20}\sum_{n=m}^{N_m}\psi_{mn}P_{mn}e^{im\phi},$$
$$\Phi_i(\theta,\phi) = \sum_{m=0}^{20}\sum_{n=m}^{N_m}V_{mni}P_{mn}e^{im\phi}, \quad \text{(C3)}$$

where ψ_{mn} and V_{mni} are the spectral coefficients. $P_{mn}(\mu)$ are the associated Legendre polynomials of the first kind of degree l and order m and where μ is the sine of the geographic latitude, which form an orthonormal set over $(-\pi/2, \pi/2)$. N_m=21 if m is even and N_m=20 if m is odd. Substitution of Eq. (C3) into Eq. (C2) yields

$$\sum_{m=0}^{20}\sum_{n=m}^{N_m}\overline{\psi_{m'n'}\psi_{mn}}V_{mni} = \lambda_i V_{m'n'i}, \quad \text{(C4)}$$

where V_{mni} is the spectral coefficient of the the i-th POD mode V_i at the spectral grid point (m, n).

Appendix D Symmetrising the eigenvector problem

Since the correlation matrix is now no longer symmetric, we need to diagonalise **CM** in Eq. (26) by introducing a symmetric matrix $\mathbf{D}=\mathbf{M}^{\frac{1}{2}}\mathbf{C}\mathbf{M}^{\frac{1}{2}}$ (where $\mathbf{M}^{\frac{1}{2}}\mathbf{M}^{\frac{1}{2}}=\mathbf{M}$), with the same eigenvalues as **CM**. We now solve

$$\mathbf{D}\mathbf{E}' = \lambda\mathbf{E}', \quad \text{(D1)}$$

where $\mathbf{E}'=\mathbf{M}^{\frac{1}{2}}\mathbf{E}$, since $\mathbf{M}^{\frac{1}{2}}\mathbf{C}\mathbf{M}^{\frac{1}{2}}\mathbf{M}^{\frac{1}{2}}\mathbf{U}=\lambda\mathbf{M}^{\frac{1}{2}}\mathbf{U}$. Having found the POD modes, we used $\mathbf{E}=\mathbf{M}^{-\frac{1}{2}}\mathbf{E}'$ to recover Euclidean spectral space, followed by a Fast Fourier Transform to transform the spatial modes back to physical grid space. Direct comparisons can then be made between the qualitative structures of each of the modes obtained from the various norms.

Edited by: T. Chang
Reviewed by: one referee

References

Achatz, U. and Branstator, G.: A two-layer model with empirical linear corrections and reduced order for studies of internal climate variability, J. Atmos. Sci., 56, 3140–3160, 1999.

Achatz, U. and Opsteegh, J.: Primitive-equation-based low-order models with seasonal cycle, Part I: Model construction, J. Atmos. Sci., 60, 465–477, 2003a.

Achatz, U. and Opsteegh, J.: Primitive-equation-based low-order models with seasonal cycle, Part II: Application to complexity and nonlinearity of large-scale atmospheric dynamics, J. Atmos. Sci., 60, 478–490, 2003b.

Andrews, D., G., Holton, J. R., and Leovy, C. B.: Mid Atmospheric Dynamics, Academic Press, 1987.

Banfield, D., Conrath, B. J., Gierasch, P. J., Wilson, R. J., and Smith, M. D.: Traveling waves in the Martian atmosphere from MGS TES nadir data, Icarus, 170, 365–403, 2004.

Barnes, J.: Time spectral analysis of midlatitude disturbances in the Martian atmosphere, J. Atmos. Sci, 37, 2002–2015, 1980.

Barnes, J.: Midlatitude disturbances in the Martian atmosphere: A second Mars year, J. Atmos. Sci, 38, 225–234, 1981.

Barnes, J., Pollack, J. B., Haberle, R. M., Zurek, R. W., Leovy, C. B., Lee, H., and Schaeffer, J.: Mars atmospheric dynamics as simulated by the NASA Ames general circulation model: II Transient baroclinic eddies, J. Geophys. Res, 98, 3125–3148, 1993.

Blackburn, M.: Program description for the multi-level global spectral model, University of Reading, Dept. of Meteorology, Atmospheric Modelling Group, 1985.

Buizza, R. and Palmer, T. N.: The singular-vector structure of the atmospheric global circulation, J. Atmos. Sci., 52, 1434–1456, 1995.

Collins, M.: The Meteorology of Mars, Ph.D. thesis, Reading, 1993.

Collins, M. and James, I.: Regular baroclinic transient waves in a simplified global circulation model of the Martian atmosphere, J. Geophys. Res., 100 (E7), 14 421–14 432, 1995.

Collins, M., Lewis, S. R., Read, P. L., and Hourdin, F.: Baroclinic wave transitions in the Martian atmosphere, Icarus, 120, 344–357, 1996.

D'Andrea, F.: Extratropical low-frequency variability as a low-dimensional problem II: Stationarity and stability of large-scale equilibria, Q. J. Roy. Meteor. Soc., 128B, 1059–1073, 2002.

D'Andrea, F. and Vautard, R.: Extratropical low-frequency variability as a low-dimensional problem I: A simplified model, Q. J. Roy. Meteor. Soc., 127B, 1357–1374, 2001.

Flierl, G. R.: Models of vertical structure and the calibration of two-layer mo dels, Dyn. Atmos. Oceans., 2, 341–381, 1978.

Gierasch, P. J. and Goody, R. M.: The effect of dust on the temperature of the Martian atmosphere, J. Atmos. Sci, 29, 400–402, 1972.

Hess, S. L.: Some aspects of the meteorology of Mars, J. Meteorol., 7, 1–13, 1950.

Hoskins, B. J. and Simmons, A. J.: A multilayer spectral model and the semi-implicit method, Quart. J. R. Met. Soc., 109, 771–783, 1975.

James, I. N.: Introduction to Circulating Atmospheres, Cambridge University Press, 1994.

Kantz, H. and Schreiber, T.: Nonlinear time series analysis, Cambridge University Press, Cambridge Nonlinear Science Series 7, 1997.

Lindzen, R. S., Batten, E. S., and Kim, J. W.: Oscillations in atmospheres with tops, Mon. Weath. Rev., 96, 3, 133–140, 1968.

Lumley, J. L.: The structure of inhomogeneous turbulent flows, in: Atmospheric Turbulence and Radio Wave Propagation, edited by: Yaglom, A. M. and Takarski, V. I., Nauka, Moscow, 166–178, 1967.

Lumley, J. L.: Transition and Turbulence, Academic Press, New York, 1981.

Mikhlin, S. G.: Variational Methods in Mathematical Physics, Pergamon Press, 1964.

Pollack, J. B., Colburn, D. S., Flasar, F. M., Kuhn, R., Carlston, L. E., and Pidek, D. C.: Properties and effects of dust particles suspended in the Martian atmosphere, J. Geophys. Res., 84, 2929–2945, 1979.

Read, P. L. and Lewis, S. R.: The Martian Climate Revisited: Atmosphere and Environment of a Desert Planet, Springer-Verlag, Berlin, ISBN: 3-540-40743-X, 2004.

Schubert, S. D.: A Statistical-Dynamical study of empirically determined modes of atmospheric variability, J. Atmos. Sci., 42, 3–17, 1985.

Selten, F. M.: Towards an optimal description of atmospheric flow, J. Atmos. Sci., 50, 861–877, 1993.

Selten, F. M.: An efficient description of the dynamics of barotropic flow., J. Atmos. Sci., 52, 915–936, 1995.

Selten, F. M.: Baroclinic empirical orthogonal functions as basis functions in an atmospheric model, J. Atmos. Sci., 54, 2099–2114, 1997.